

## RESEARCH ARTICLE

# Nucleus accumbens projections: Validity and reliability of fiber reconstructions based on high-resolution diffusion-weighted MRI

Thilo Rusche<sup>1,2</sup>  | Jörn Kaufmann<sup>3</sup> | Jürgen Voges<sup>1</sup>

<sup>1</sup>Department of Stereotactic Neurosurgery, Otto-von-Guericke University Magdeburg, Magdeburg, Germany

<sup>2</sup>Department of Radiology, Clinic of Radiology & Nuclear Medicine, University Hospital Basel, University Basel, Basel, Switzerland

<sup>3</sup>Department of Neurology, Otto-von-Guericke University Magdeburg, Magdeburg, Germany

## Correspondence

Thilo Rusche, Department of Stereotactic Neurosurgery, Otto-von-Guericke University Magdeburg, Leipziger Straße 44, 39120 Magdeburg, Germany.  
Email: rusche.thilo@gmail.com

## Abstract

Clinical effects of deep brain stimulation are largely mediated by the activation of myelinated axons. Hence, increasing attention has been paid in the past on targeting white matter tracts in addition to gray matter. Aims of the present study were: (i) visualization of discrete afferences and efferences of the nucleus accumbens (NAc), supposed to be a major hub of neural networks relating to mental disorders, using probabilistic fiber tractography and a data driven approach, and (ii) validation of the applied methodology for standardized routine clinical applications. MR-data from 11 healthy subjects and 7 measurement sessions each were acquired on a 3T MRI-scanner. For probabilistic fiber tracking the NAc as a seed region and the medial prefrontal cortex (mPFC), anterior cingulate cortex (ACC), amygdala (AMY), hippocampus (HPC), dorsomedial thalamus (dmT) and ventral tegmental area (VTA) as target regions were segmented for each subject and both hemispheres. To quantitatively assess the reliability and stability of the reconstructions, we filtered and clustered the

**Abbreviations:** A24, Area 24; ABmc, accessory basal nucleus magnocellular division; ABp, accessory basal posterior; ABpc, accessory basal nucleus parvocellular division; ac, accumbens frontal fasciculus; ACC, anterior cingulate cortex; Ac, accumbens frontal fasciculus; Acr, anterior corona radiata; AD, anterior dorsal nucleus; aic, anterior limb of the internal capsule; AL, agranular insular; al, Ansa lenticularis; AMY, amygdala; APC, posterior limb of the anterior commissure; AV, anterior ventral nucleus; Ba, basal anterior; BLA, basolateral amygdala; BLM, basomedial amygdala; Bmc, basal nucleus magnocellular division; Bmec, basal nucleus medio-cellular division; BNSM, bed nucleus of stria medullaris; BNST, bed nucleus of stria terminalis; Bp, basal posterior; Bpc, basal nucleus parvocellular division; CA, cornu ammonis; cc, corpus callosum; cC, cingulate cortex; Cd, nucleus caudatus; Cdm, medial caudate nucleus; Ce, central nucleus of amygdala; CG, pontomesencephalic central gray; CL, central lateral nucleus; CIN, central linear nucleus; CM, central nucleus of the meddial thalamus; COA, cortical nucleus amygdala; CPu, Claustrum-Putamen; CS, superior central nucleus; CSD, constrained spherical deconvolution; CTA, cortical amygdaloid transition area; CVLM, caudal ventrolateral medulla; DB, diagonal band; DBS, deep brain stimulation; DH, dorsal hypothalamic area; dmT, dorsomedial thalamus; dmTN, dorsal midline thalamic nucleus; DTI, diffusion tensor imaging; DWI, diffusion-weighted MRI; EN, endopiriform nucleus; EpN, endopeduncular nucleus; FLAIR, fluid attenuated inversion recovery; FOD, fiber orientation distribution; FuG, fusiform gyrus; GP, globus pallidus; HFec, hippocampal formation/entorhinal cortex; HFpc, hippocampal formation/perirhinal cortex; HFps, hippocampal formation/prosubiculum; HFS, hippocampal formation/subiculum; HPC, hippocampus; IAM, interanteromedial nucleus; IAPC, posterior limb of the anterior commissure; ICA, infralimbic cortical area; ifo, inferior longitudinal fasciculus; IF, interfascicular nucleus; IMD, intermediodorsal nucleus; IoC, islands of Calleja; LC, caudal linear nucleus; LC, locus coeruleus; lCdl, large cell division lateral nucleus of amygdala; Ldl, dorsolateral division; LDT, laterodorsal tegmental nucleus; lenf, fasciculus lentiformis; LH, lateral hypothalamus; LHA, lateral hypothalamic area; Lhb, lateral habenula; LP, lateral pulvinar nucleus; LP, lateroposterior nucleus; LR, rostral linear nucleus; LSN, lateral septal nucleus; Lvl, ventrolateral division; MDD, major depression disorder; mdTN, mediodorsal thalamic nucleus; MeAD, medial nucleus anterodorsal part; MePD, medial nucleus posterodorsal part; MFB, medial forebrain bundle; MI, primary motor cortex; MO(G), medial orbital cortex; MOPFC, medial orbital prefrontal cortex; mPFC, medial prefrontal cortex; MT, mesencephalic tegmentum; Na, nucleus arcuatus; NAc, nucleus accumbens; racc, rostral anterior cingulate cortex; RACC, rostral agranular insular cortex; Re, nucleus reuniens; RF, retrorubal field; RH, rhomboid nucleus; RN, raphe nucleus; Rs, rhinal sulcus; RTN, reticular thalamic nucleus; RVLM, rostral ventrolateral medulla; Sc, supra-chiasmatic nucleus; scdL, small cell division lateral nucleus of amygdala; SI, substantia innominata; SFG, superior frontal gyrus; SG, gyrus rectus; sm, stria medullaris of thalamus; SN, substantia nigra; SSTI, substriatal terminal island; STN, nucleus subthalamicus; Str, stria terminalis; SuMn, supramammillary nucleus; sumx, supramammillary commissure; TM, tuberomammillary nucleus; TP, timepoint; TPP, nucleus tegmenti pedunculopontinus; unc, fasciculus uncinatus; VC, ventral branch of the diagonal band; vHC, ventral hippocampus; VMH, ventromedial hypothalamic nucleus; dorsomedial part, ventrolateral part; VO, ventral orbital cortex; VOI, volume of interest; VP, ventrales pallidum; VT/VS, ventral striatum; VTA, ventral tegmental area; WP, waypoint.

This is an open access article under the terms of the Creative Commons Attribution License, which permits use, distribution and reproduction in any medium, provided the original work is properly cited.

© 2021 The Authors. *Human Brain Mapping* published by Wiley Periodicals LLC.

individual fiber-tracts (NAc to target) for each session and subject and performed a point-by-point calculation of the maximum cluster distances for intra-subject comparison. The connectivity patterns formed by the obtained fibers were in good concordance with published data from tracer and/or fiber-dissection studies. Furthermore, the reliability assessment of the (NAc to target)-fiber-tracts yielded to high correlations between the obtained clustered-tracts. Using DBS with directional lead technology, the workflow elaborated in this study may guide selective electrical stimulation of NAc projections.

#### KEYWORDS

deep brain stimulation, diffusion-weighted MRI, nucleus accumbens, projections

## 1 | INTRODUCTION

The NAc as the major component of the ventral striatum (VS) is a key relay in the mesolimbic, dopaminergic reward system with strong connections to the amygdala (AMY), dorsomedial thalamus (dmT), ventral tegmental area (VTA), hippocampus (HPC) and to the neocortex comprising the anterior cingulate cortex (ACC) and the orbital and the medial prefrontal cortex (OFC, mPFC) (Haber & McFarland, 1999).

Brain areas such as the dorsal ACC (dACC), OFC, ventro-medial (vm) PFC and AMY were specifically related to the pathophysiology of psychiatric disorders (Haber & Behrens, 2014; Ressler & Mayberg, 2007). Hence NAc and VS are supposed to be a major hub within these networks and have already been used as a target to treat obsessive compulsive disorder (OCD), major depressive disorder (MDD) or addiction with deep brain stimulation (DBS) (Bewernick, Kayser, Sturm, & Schlaepfer, 2012; Denys et al., 2010; Sturm et al., 2003; Voges, Muller, Bogerts, Munte, & Heinze, 2013). In addition, NAc-DBS improved substantially partial epilepsy in an open labeled case series and a randomized controlled case series (Kowski et al., 2015; Schmitt et al., 2014).

The clinical efficacy of DBS bases mainly upon the activation of myelinated axons leading to local but also network-wide electrical and neurochemical effects with modification of the oscillatory activity of neurons, synaptic plasticity or the degree of synchronization between different brain areas (Herrington, Cheng, & Eskandar, 2016; Udupa & Chen, 2015). Hence, the first goal of the present study was to visualize in the brain of healthy individuals selectively those neural projections connecting the NAc with the abovementioned brain regions using diffusion-weighted MR imaging (DWI) and probabilistic fiber tractography. The target regions were selected on the basis of a detailed data analysis from anatomical tracer studies (brain of rodents, pigs or non-human primates) and from fiber-dissection studies (human brains) with regard to the functionally and anatomically most important NAc afferents and efferents. The second goal of the present study was to demonstrate the validity and reliability of our methodological approach and to develop a standardized workflow for the routine application in patients.

## 2 | MATERIALS AND METHODS

### 2.1 | Literature review

The Pubmed-based literature research was performed using the following search combinations (abstract/title) up to and including June 2021: “NAc AND connections,” “NAc AND efferents,” “NAc AND afferents,” “NAc AND DTI,” “NAc AND tract tracing,” “NAc AND projections” and “NAc AND networks.” The search was limited to publications in English language and anatomical studies performed on non-human primates, pigs, mice, or rats using either chemical fiber tract-tracing or autoradiography. We tabularly summarized the collected data and compared them with the database on [www.bams1.org](http://www.bams1.org). Afterwards a graphic illustration was implemented with the free-ware tool *RAWGraphs* on [www.rawgraphs.io](http://www.rawgraphs.io). To define clinically relevant NAc-connections we finally identified those projection areas, whose dysfunction is supposed to be causative related to the symptoms of OCD, MDD or addiction (Giacobbe, Mayberg, & Lozano, 2009; Heimer, 2003; Milad & Rauch, 2012).

### 2.2 | MRI-datasets and segmentation

#### 2.2.1 | MRI data acquisition

Eleven healthy subjects (five female, six male, ten right-handed, one left-handed, average age: 29.1 years) gave their informed consent (positive vote from the ethics committee of the Otto-von-Guericke-University Magdeburg; approval number: 106/98) for cranial MRI-examinations. In each case, we repeated the examinations seven times as separate sessions using a Siemens *MAGNETOM Prisma* 3T-scanner, the software *Syngo D13D* and a standard 64-channel phased array imaging coil in receive mode (for specific measurement parameters see Table 1; for more detailed explanation of performed steps see Figure 1). To increase inter-subject reproducibility in position and minimize motion a pillow was placed surrounding the sides and the back of the head. The field of view was aligned in all diffusion scans to the anterior commissure (AC)–posterior commissure



an unweighted volume. In total, 120 diffusion-weighted volumes ( $b = 1,000 \text{ s/mm}^2$ ) and 13 non-diffusion-weighted volumes ( $b = 0 \text{ s/mm}^2$ ) were obtained in each session. The overall measurement time for each individual was about 6 hr.

## 2.2.2 | Region-of-interest (target) segmentation

We defined clinically relevant targets as mentioned above and segmented these targets. NAc, HPC, AMY and dmT were manually segmented within the T1-weighted single-subject-template, the VTA within the FLAIR-single-subject-template separately for the left and right hemisphere using *FSL-Viewer* (FMRIB Software Library, Release 5.0.9 [Jenkinson, Beckmann, Behrens, Woolrich, & Smith, 2012]; The University of Oxford). Reference for the definition of landmarks for each target was the “Atlas of the human brain” (Mai, Voss, & Paxinos, 2008). A computer-based, automated target segmentation was carried out for the cortical areas ACC and mPFC using a *Freesurfer* software package (version 5.3) (Dale, Fischl, & Sereno, 1999).

## 2.3 | Diffusion-weighted MRI based fiber-reconstructions and visualization of selective NAc-connections

### 2.3.1 | MRI-data preprocessing and target-mask transformation

DICOM to NIFTI conversion was carried out using *MRICron's dcm2nii* (<http://people.cas.sc.edu/rorden/mricron>). Next, diffusion data were preprocessed using *dwidenoise* and *mrdegibbs* with a program package of *MRtrix* ([Kellner, Dhital, Kiselev, & Reisert, 2016; Tournier et al., 2019]; [www.mrtrix.org](http://www.mrtrix.org)). To correct for eddy-current-induced distortions, the diffusion-weighted images were registered to a corresponding b0-image based on a 12-dof affine transformation using FSL-tool *eddy\_correct* with spline interpolation (Graham, Drobnyak, & Zhang, 2016). To account for head movement, an affine transformation from each block's non-diffusion-weighted volume to the first b0-image using FSL-tool *flirt* (Jones & Cercignani, 2010; Smith et al., 2004). The DWI data of each block were then realigned based on these transformations. Geometric distortions induced by magnetic field inhomogeneities were corrected based on the GRE field map, and the diffusion data were registered to the corresponding T1-weighted image. These steps (EPI distortion correction and EPI-to-MPRAGE registration) were performed simultaneously using FSL-tool *epi\_reg*. Finally, a mask consisting of non-weighted diffusion-data was calculated only containing the brain (brain-mask) with FSL-tool *bet*. In the following steps based on the *MRtrix3* software package using *dwi2response* response functions from the preprocessed diffusion-weighted images and fiber orientation distributions (FOD) with *dwi2fod* using constrained spherical deconvolution (CSD) were estimated.

The target-masks were transformed from each T1/FLAIR-single-subject-template volume into the corresponding subject diffusion-

weighted data space with the program package *ANTs* (*WarpImageMultiTransform* [Avants et al., 2010]) as a composite function of three (T1-template → MPRAGE, MPRAGE → diffusion-weighted data [affine + nonlinear transformation]) (T1) respective four transformation steps (*FLAIR*) (*FLAIR* → T1-template transformation additionally).

### 2.3.2 | Fiber-tracking: Graphic visualization of DWI-datasets with MRtrix

All generated target masks could be used as a fiber-tracking seed or target region. Graphical notation of the datasets was realized with the program *MRtrix*. Using *tckgen*, a minimum of 100,000 and a maximum of  $10^7$  starts were generated outgoing from the start regions. A probabilistic, unidirectional fiber tracking procedure and standard parameters were used (algorithm *iFOD2*, Proc. Intl. Soc. Mag. Reson. Med. 18 [2010]). Moreover, versions with (ACT-version (information of the distribution of white and gray matter) (Smith, Tournier, Calamante, & Connelly, 2012)) or without anatomic information were considered. For every seed to target connection, we defined a maximum fiber-length: ACC 55 mm, AMY 40 mm, HPC 65 mm, mPFC 55 mm, dmT 30 mm and VTA 30 mm.

Next, we generated FA-single-subject-templates using the FA-maps of timepoint 1–7 for each subject (*ANTs*, *Multivariate TemplateConstruction 2*). Then, the fiber-coordinates were transformed to the single-subject-space (*ANTs* and *MRtrix* with command *tcktransform*) utilizing the linear (affine) and nonlinear (*Warp-fields*) transformations.

Afterwards, paths with similar properties (i.e., trajectories, length) were grouped into clusters of paths using a clustering algorithm implemented in Matlab (Mathworks, Natick, MA) with the following criteria:

- The start- and endpoint as well as two equidistant points along the path must not exceed a spatial Euclidian distance of 10 mm.
- The difference in path-lengths must not be greater than 10%.

With some NAc-target connections (mPFC, ACC and HPC) a so-called filtering of the fiber-tracts was necessary before the clustering process. This was always the case when fiber-tracts (even after optimizing the maximum fiber-length) had partially inhomogeneous path courses over contralateral structures (especially anterior commissure) or several path segments and the clustered fiber-tracts would therefore be inconsistent or significantly divergent. In detail (like the ROI-definition for the target masks), a fiber-tract-specific ROI for both hemispheres was segmented into the FA-single-subject-templates. The ROIs ( $2 \times 2$  pixels) were segmented in coronal slices for both hemispheres:

- Within the fiber-pathway of the anterior corona radiata (acr) shortly before the distribution in the gyrus rectus (SG) and superior frontal gyrus (SFG) for the NAc-mPFC-connection.

2. At the level of the crossing point of the ventral/dorsal ACC at the level of the genu corporis callosi for the NAc-ACC-connection.
3. Within the distal part of the stria terminalis (str) for the NAc-HPC-connection.

The visualization of the paths was conducted with the MRtrix viewer *mrview* using seven single measurements/datasets of a representative sample subject (see Figures 3–10). In order to generate comparable coordinates with regard to the common literature (especially in comparison to the Mai-Atlas [Mai et al., 2008]), the T1-template was transferred to a coordinate system whose *y*-axis corresponds to the AC-PC-line with the AC as origin (0|0|0) (*x*-axis from left to right and *z*-axis from inferior to superior). All defined waypoints (WP; representative and path-specific point of fiber-tract) (see Figures 3–10) are denoted in this system. In particular, the distance between the AC and PC of the brain of the Mai-Atlas (approx. 28 mm) was comparable with that of the sample subject (approx. 26 mm). This additionally ensures good transferability of the data to the generally valid Mai-Atlas.

## 2.4 | Evaluation of fiber-tracts reliability and stability

The statistical evaluation based on the 924 NAc to target single-fiber-connections of subject 1–11 for timepoint 1–7 and both hemispheres with the ACT-algorithm (see above).

### 2.4.1 | Intra-subject-comparison

Optimal stereotactic treatment planning depends to a large proportion on the quality of the underlying MRI-images, in the present case on the reliability and stability of the calculated fiber-tracts. To determine this variable, we performed a quantitative comparison of the single-fiber-connections for all NAc to target pathways and a qualitative-visual comparison exemplarily for the NAc to mPFC connections.

For the qualitative-visual-comparison, we visualized the NAc to mPFC fiber-connections for each subject (1–11) and timepoint (1–7) in the left hemisphere using *MRview*. Next, we determined the AC on axial slices of the generated MRI-datasets as an anatomical reference point. Finally, with the help of *Inkscape* (version 0.92.2) screenshots of the displayed fiber-connections were tabularly arranged (row: subject 1–11; column: timepoint 1–7).

Quantitative comparison was performed by generating a trajectory for each clustered main-pathway (pathway with the most identical fiber-connections) (see Section 2.3.2) of each NAc-target connection (mPFC, ACC, HPC, AMY, VTA and dmT) for each session 1–7 and each subject 1–11. The trajectory was calculated by determining the centroid-path from the coordinates of all individual paths within the cluster. In a next step the shortest trajectory was selected and the

Euclidian distances to each other trajectories were calculated point-by-point. The different distances were then saved and plotted (*x*-axis: steps in the clustered paths [0.8 mm per step]); *y*-axis: distance to the shortest cluster in mm). Finally, the following values were also calculated and summarized in a table (see Section 3.2.1 and Figure 15):

1. The maximum Euclidian distances of single-clusters to the shortest single-cluster (maximum distance of a single-cluster to the shortest single-cluster per session [measurement timepoint] and subject and NAc-target connection per hemisphere).
2. The average maximum Euclidian distances of single-clusters to the shortest single-cluster (average maximum distances of single-clusters for session 1–7 of a subject 1–11 per NAc-target connection and hemisphere).
3. Maximum mean distances (average maximum distance of single-clusters for all subjects 1–11 and sessions 1–7 per NAc-target connection and hemisphere).

### 2.4.2 | Inter-subject-comparison using the example of the NAc to mPFC fiber-connections

Accuracy and fidelity to reality of the reconstruction of NAc fiber-connections depends on the identification and accordance of fiber-tract-specific waypoints. To determine these variables, we performed a qualitative-visual inter-subject-comparison of the NAc to mPFC single-fiber-connections of subject 1–11 by preparing and analyzing a tabularly overall image as described in Section 2.3.1.

## 3 | RESULTS

### 3.1 | Literature analysis

The defined search combinations led to the following hits: “NAc AND connections”: 397, “NAc AND efferents: 113, “NAc AND afferents”: 379, “NAc AND DTI”: 53, “NAc AND tract tracing”: 48, “NAc AND projections”: 979, and “NAc AND networks”: 401. After filtering 207 manuscripts remained. 58 out of search combination one, 6 out of two, 47 out of three, 0 out of four, 12 out of five, 82 out of six and 1 out of seven. From each of the remained publications we extracted the observed NAc projections and documented them tabularly. In a second step, we displayed the numbers of the various NAc-afferents (NAca) and efferents (NAce) in a graph (Figure 2). The width of the individual lines, graphically represented in different colors, was greater the more often the corresponding single-connection was described in the manuscripts we examined. Thalamus, Amygdala, Hypothalamus, Hippocampus, Optic area (OA) and anterior Commissure (AC) were additionally divided into sub-regions. The most frequently described connections were from NAc to Thalamus (151), AMY (79), VTA (56), HPC (54), Hypothalamus (54), SN (36), PFC (30), and VP (26).

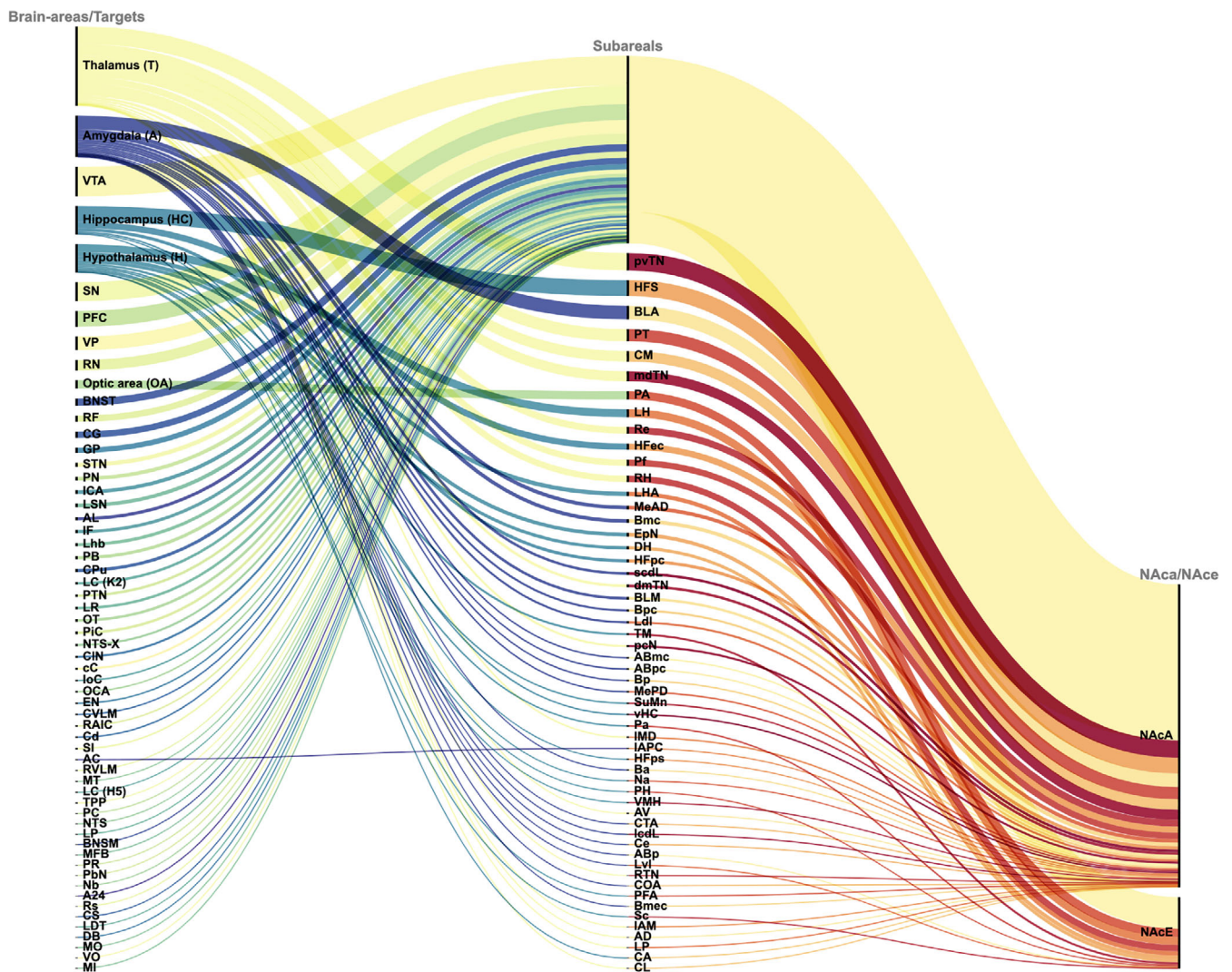


**FIGURE 2** Quantitative visualization of NAc-projections according to the results of published tracer studies

### 3.2 | Diffusion-weighted-MRI based fiber-reconstructions and visualization of selective NAc-connections

We were able to construct a fiber-tract with *MRtrix* including fiber-tracking with or without ACT as well as reverse tracking (target as seed region, NAc as target region) for each individual NAc-to-target-connection. In total, we generated 3,080 fiber-tracts. Independent from the applied method (with ACT, without ACT and reverse) each NAc-to-target connection lead to qualitatively the same fiber-patterns which were thoroughly consistent with the published anatomic data. The following description of fiber-pathways connecting the NAc with the AMY, ACC, dmT, HPC, mPFC and VTA summarizes the information, which we extracted from MRI-based fiber-tracking. For the description of the 3D-orientation we used the forebrain axis (Forel's axis) with the directional terms rostral-caudal/posterior and dorsal-ventral, respectively (Forel et al., 1875). The indicated anatomical landmarks refer to the "Atlas of the human brain" published by Mai & Paxinos (Mai et al., 2008).

#### 3.2.1 | NAc to AMY (Figure 3)

The main fiber bundles originated directly from posterior parts of the NAc (WP1, Figure 3). Smaller fibers originating from central parts of the NAc joined with these main bundles throughout their further common course. Afterwards, the fibers passed posterolateral into the Ansa lenticularis-pathway (WP2; Figure 3). Most of the fibers entered posterolateral parts of the AMY projecting onto the basal and central amygdala nuclei (WP3, Figure 3).

#### 3.2.2 | NAc to ACC (Figure 4)

The majority of fibers connecting the NAc with the ACC originated in rostro-ventro-medial parts of the NAc (WP1, Figure 4). Then, the fibers followed the ventral branch of the diagonal band (VDB) to the rostral fiber-parts of the Corpus callosum (cc) (WP2, Figure 4). From the rostrum of the cc the fibers reached the Gyrus cinguli performing the typically falciform configuration of that gyrus (WP3, Figure 4).

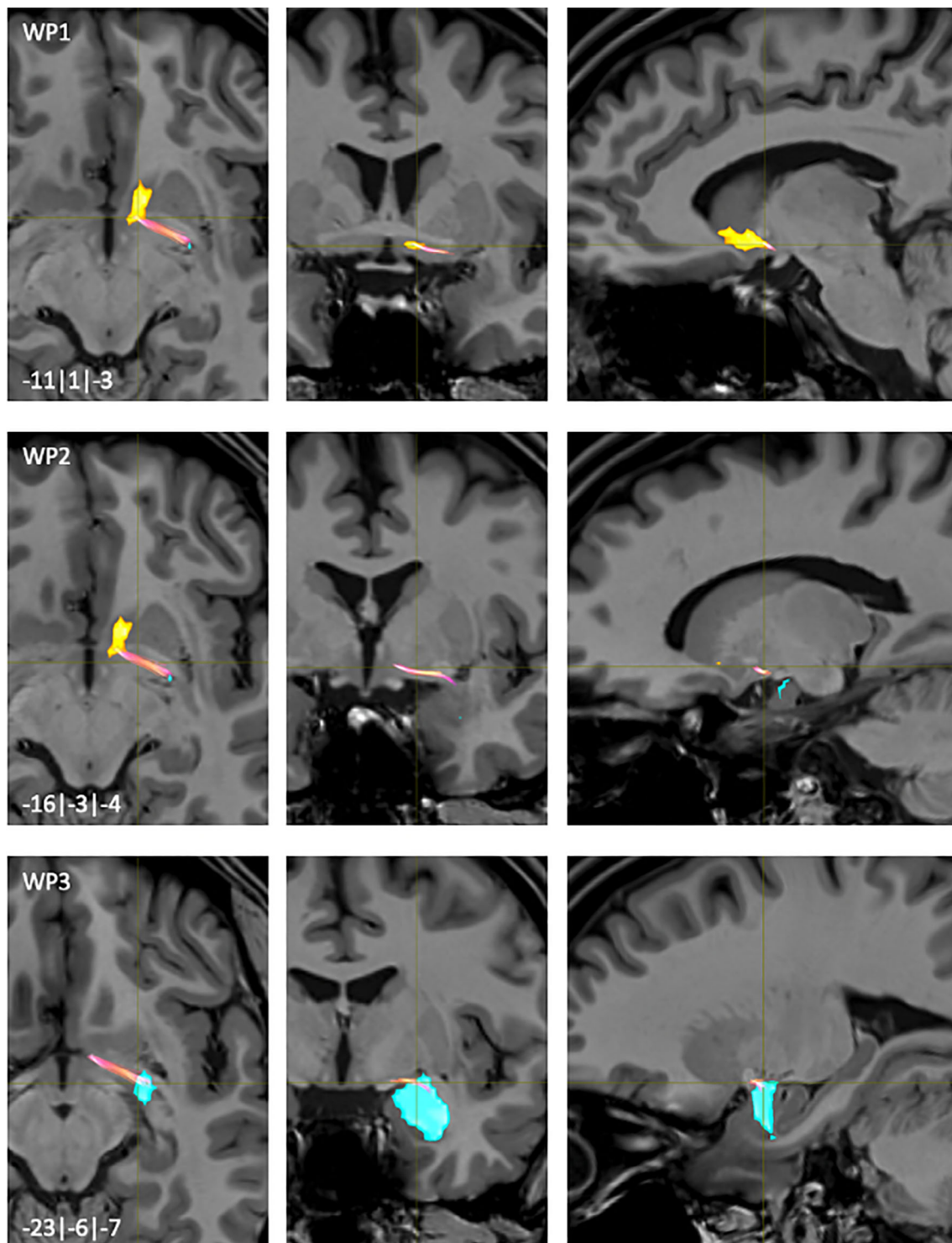


**FIGURE 3** NAc to Amygdala fiber-tract for left hemisphere: Waypoints 1–3 and distance to AC (0|0|0) in mm (x|y|z) = (left(–)/right|posterior (–)/anterior|inferior(–)/superior); yellow surface: NAc, light blue surface: Amygdala

### 3.2.3 | NAc to mdT (Figure 5)

We identified a fiber-pathway, which originated in rostralateral parts of the NAc and had a straight course posterior and parallel to the anterior limb of internal capsule (aic) (WP1, Figure 5). The fibers of

this pathway continued inside the lateral wall of the third ventricle in dorsal-posterior direction projecting mainly onto the paraventricular thalamic nucleus (pvTN) and stria medullaris of thalamus (sm). This pathway entered the dorsal and ventral parts of the medial thalamus from medial (WP2, Figure 5).

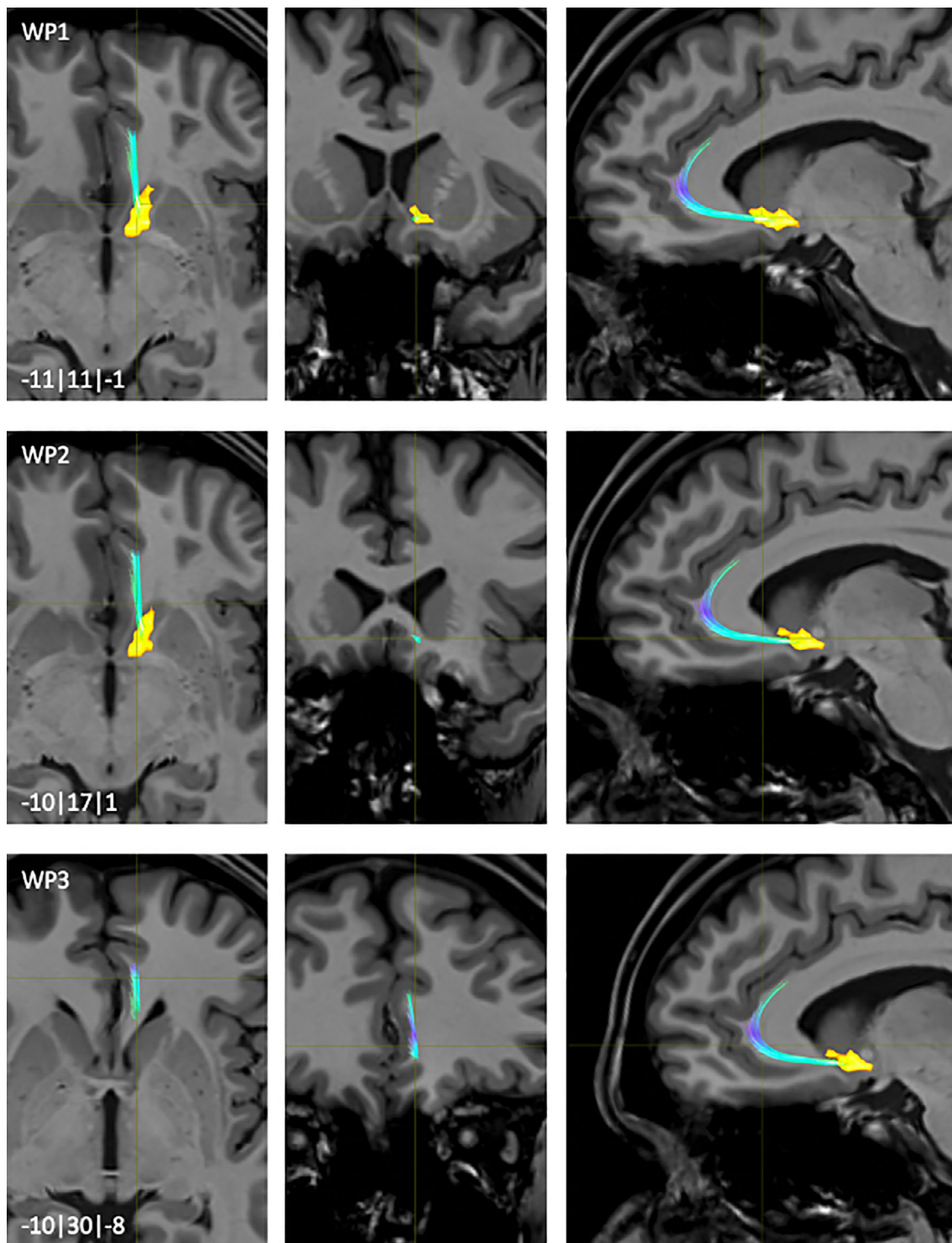


**FIGURE 4** NAc to ACC fiber-tract for left hemisphere: Waypoints 1–3 and distance to AC (0|0|0) in mm (x|y|z) = (left(–)/right|posterior (–)/anterior|inferior(–)/superior); yellow surface: NAc

### 3.2.4 | NAc to HPC (Figures 6 and 7)

The NAc to HPC fibers emerged from dorsocaudal areas of the NAc (WP1, Figure 6) with a short lateral course together with the AC. From that point on they were divided in two tracts. The medial one went

caudomedially passing the Fasciculus lenticularis (lenf) (WP2, Figure 6) and followed fibers of the Stria terminalis (str) (WP3, Figure 6). Another more lateral fiber-tract passed from the AC ventro-lateral within the fiber-pathway of the Ansa lenticularis (al) (WP4, Figure 7) before terminating mainly into posterolateral parts of the HPC (WP5, Figure 7).

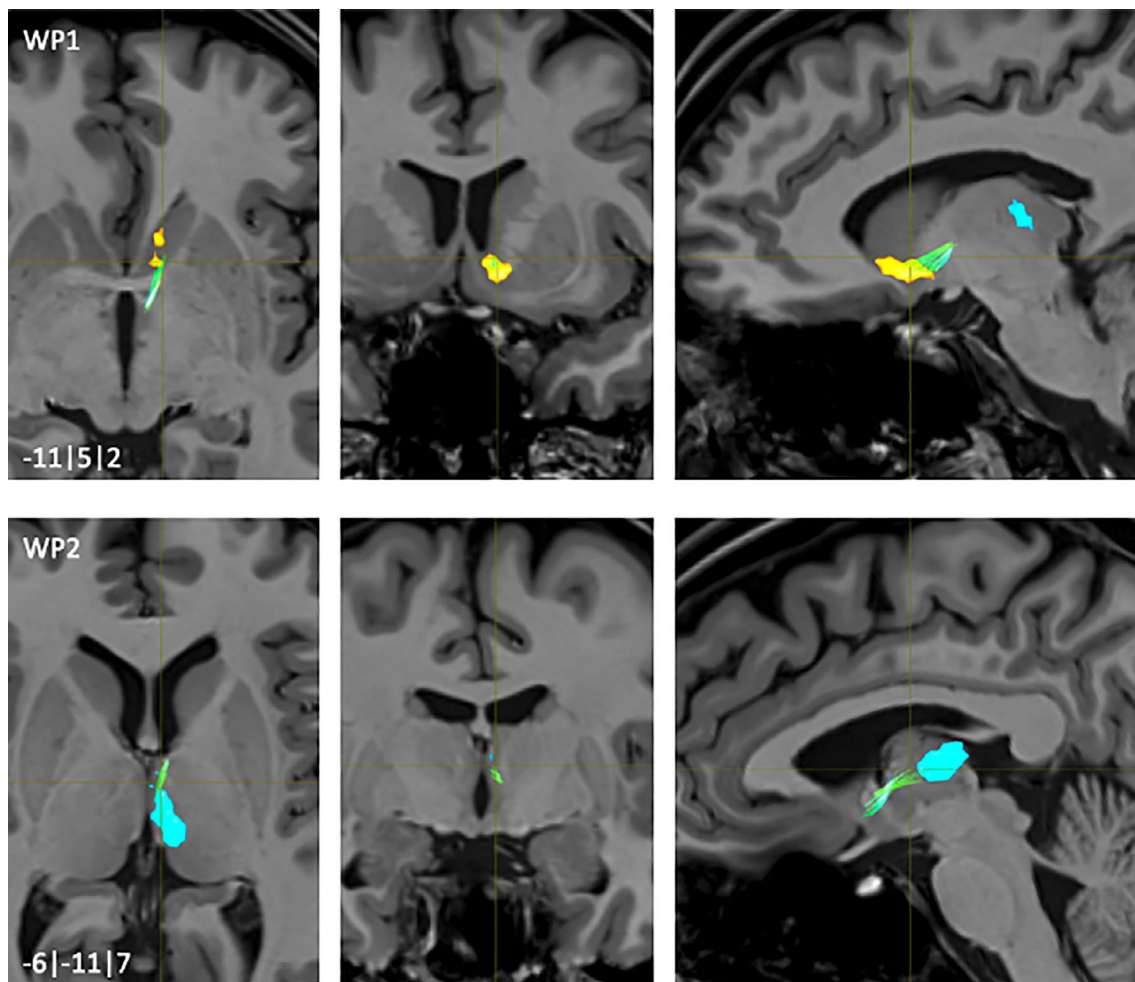


**FIGURE 5** NAc to mdT fiber-tract for left hemisphere: Waypoints 1–2 and distance to AC (0|0|0) in mm (x|y|z) = (left(-)/right|posterior (-)/anterior|inferior(-)/superior); yellow surface: NAc; light blue surface: dmT

### 3.2.5 | NAc to mPFC (Figures 8 and 9)

The connections from the NAc to the mPFC were divided into a medial and a lateral fiber-pathway (WP1, Figure 8). The medial pathway projected onto the accumbens-frontal fascicle (ac) (Rigoard et al., 2011). Starting from ventromedial, predominantly from rostromedial parts of the NAc, the course of this tract was in rostral direction (WP2, Figure 8). The majority of the fibers approached the Gyrus rectus (SG) and superior frontal gyrus (SFG) via fibers of the anterior corona radiata (Acr) (WP3/4, Figures 8 and 9). Some fibers also ended within parts of the medial orbital gyrus (MOG).

The lateral fiber-pathway started mainly from dorsolateral parts of the rostral half of the NAc (WP5, Figure 9). After their rostral course, the main part of the fibers approached the MOG in the region of the medial orbital PFC (MOPFC).

### 3.2.6 | NAc to VTA (Figure 10)

These connections had starting points in dorso-caudo-lateral and posterior compartment of the NAc (WP1, Figure 10). Fibers emerging from the dorso-caudo-lateral NAc extended straightly into posterior

direction within fibers of the ventral part of the anterior limb of the internal capsule (vaic) located between the NAc and ventral putamen (WP2, Figure 10) reaching more ventro-posteriorly the dorsal hypothalamus (DH). Fibers emerging from the posterior NAc merged with the dorso-rostro-lateral fibers at the level of the DH (WP3, Figure 10) before ending together within the VTA. Another third small fiber-pathway became visible on coronal slices emerging from the supramammillary commissure (sumx) to rostro-dorso-medial parts of the VTA (WP4, Figure 10). Some of these fibers projected onto the mesencephalon but did not end in the VTA. These structures represented most likely artifacts.

## 3.3 | Fiber-tract reliability and stability

### 3.3.1 | Intra-subject-comparison

In general, the qualitative-visual intra-subject-comparison of the NAc to mPFC fiber-connections and quantitative intra-subject-comparison of all NAc to target connections (NAc → mPFC, NAc → ACC, NAc → HPC, NAc → AMY, NAc → VTA, NAc → dmT) could be executed for each session (measurement timepoint) 1–7 and subject 1–11.

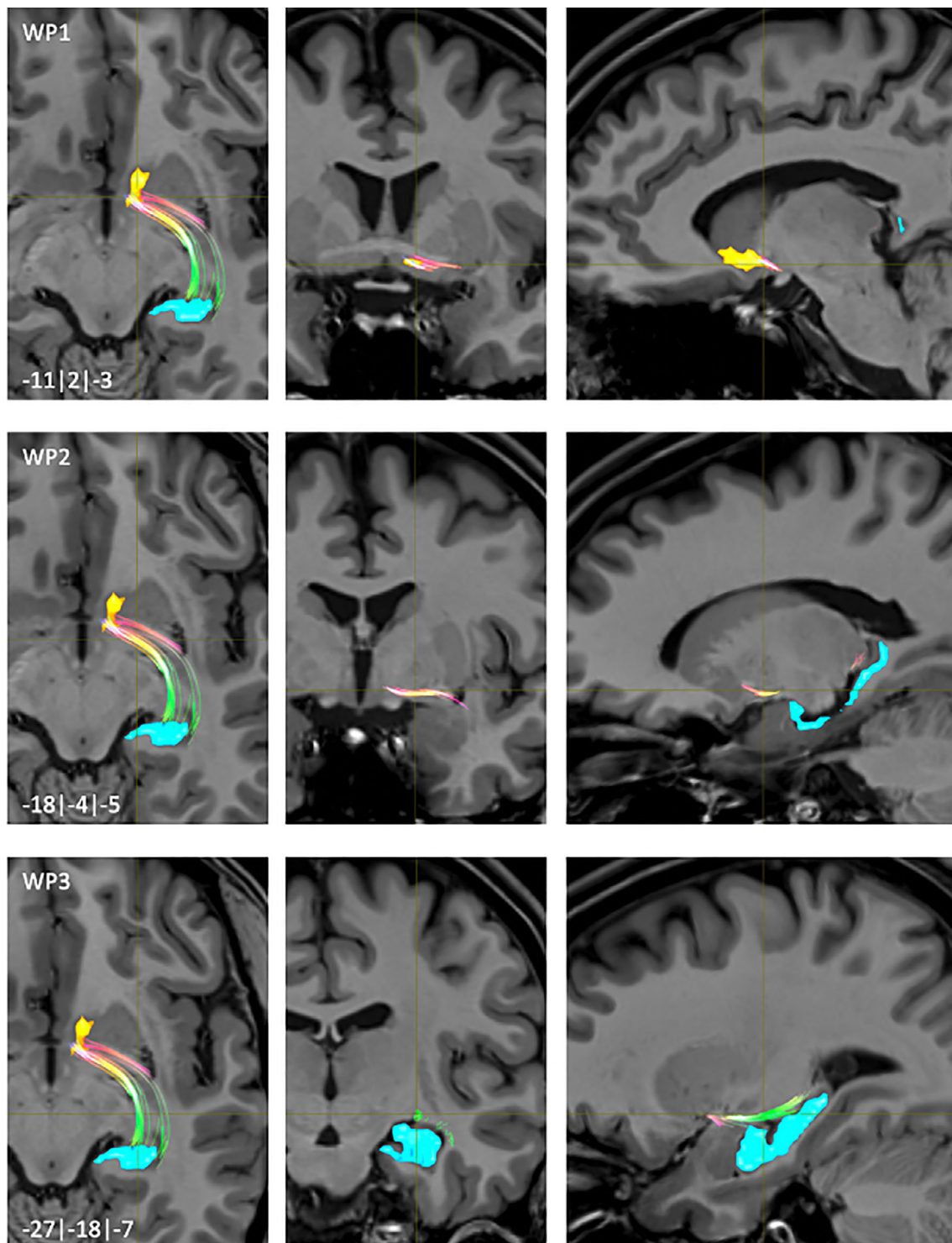


**FIGURE 6** NAc to hippocampus fiber-tract for left hemisphere: Waypoints: 1–3 and distance to AC (0|0|0) in mm (x|y|z) = (left (-)/right|posterior(-)/anterior|inferior(-)/superior); yellow surface: NAc, light blue surface: hippocampus

**a. Qualitative-visual intra-subject-comparison of the NAc to mPFC fiber-connections**

Figures 11 and 12 illustrate the NAc to mPFC fiber-connections of the left hemisphere for each subject 1–11 for timepoints 1–7 in axial slices at the level of the AC. This image shows a broad

accordance among subjects for all fiber-trajectories described under point 3.1.5. Minor deviations were related to the representation of a contralateral fiber-pathway over the AC (compare as an example Figure 11 subject 1 TP 1,2,3,4,6,7 with TP 5) or were expressed by differences of the visually-quantitatively recorded

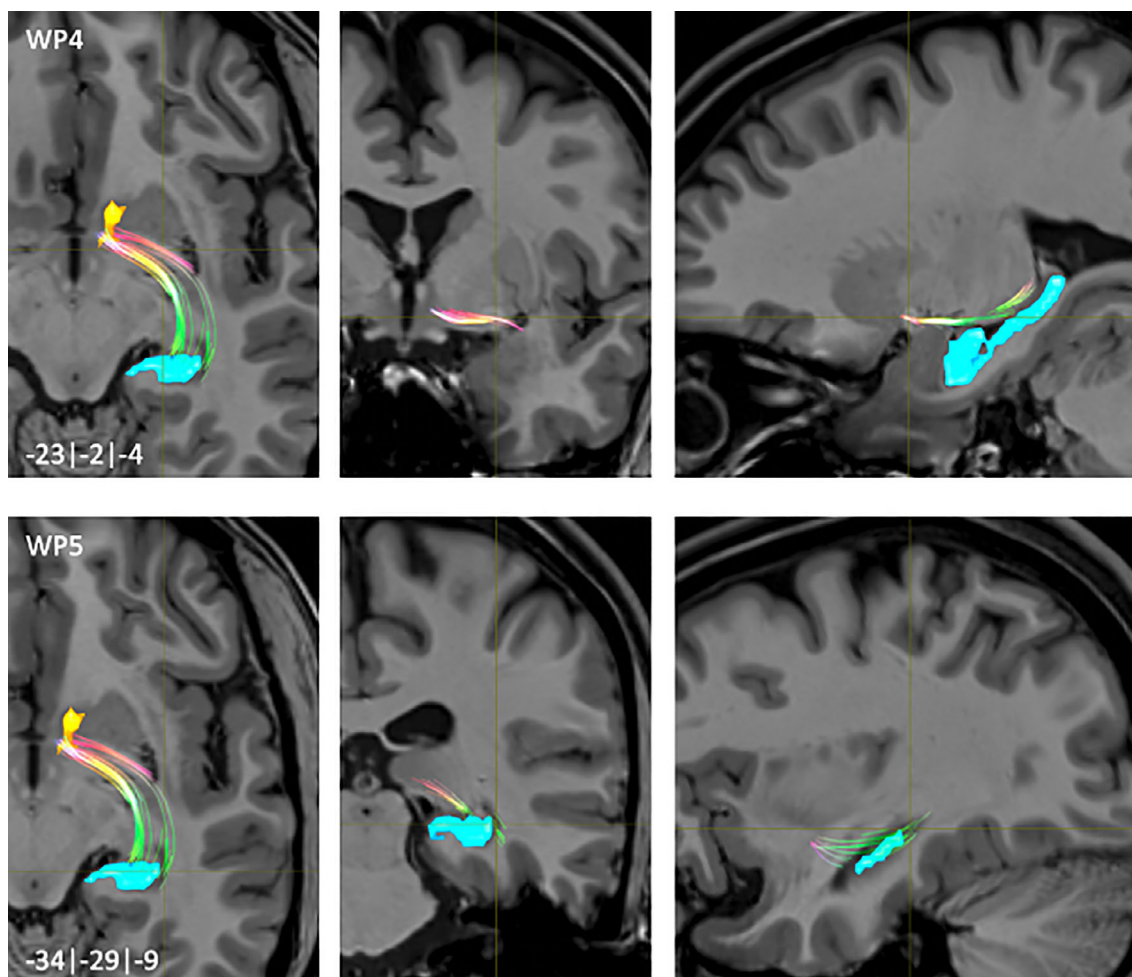


**FIGURE 7** NAc to hippocampus fiber-tract for left hemisphere: Waypoints: 4–5 and distance to AC (0|0|0) in mm (x|y|z) = (left (-)/right|posterior(-)/anterior|inferior(-)/superior); yellow surface: NAc, light blue surface: hippocampus

total fiber quantity within an ROI (compare fiber quantity at the level of Gyrus rectus and MOG between TP 3 and 4 of subject 5 in Figure 11).

**b. Quantitative intra-subject-comparison of all NAc to target connections**

Within the quantitative intra-subject-comparison, the following maximum Euclidian distances from single-cluster to the shortest single-cluster could be determined for the individual NAc-target connections (see Figure 15): ACC 3.97 mm (subject 10, right hemisphere), AMY 3.13 mm (subject 3, right hemisphere), dmT 5.71 mm (subject 7, left hemisphere), HPC 5.5 mm (subject 8, left hemisphere), mPFC 4.31 mm (subject 9, left hemisphere) and VTA 6.35 mm (subject 7, left hemisphere). The average maximum Euclidian distances of the single-clusters to the shortest single-cluster for the individual NAc-target connections were (see Figure 15): ACC 1.57 mm (subject 5, right hemisphere), AMY 2.15 mm (subject 5, right hemisphere), dmT 3.45 mm (subject 2, left hemisphere), HPC 2.15 mm (subject 8, right hemisphere), mPFC 3.02 mm (subject 5, left hemisphere) and VTA 3.83 mm (subject 7, left hemisphere). The maximum mean distances (average maximum distance of single-

clusters for all subjects 1–11 and TP 1–7 per NAc-target-connection) were as follows (see Figures 13–15): NAc-ACC 1.00 mm left and 0.98 mm right hemisphere, NAc-AMY 0.94 mm left and 1.01 mm right hemisphere, NAc-dmT 1.67 mm left and 1.70 mm right hemisphere, NAc-HPC 1.01 mm left and 0.99 mm right hemisphere, NAc-mPFC 1.07 mm for both hemispheres and NAc-VTA 2.26 mm left and 1.98 mm right hemisphere.

**3.3.2 | Inter-subject-comparison using the example of the NAc to mPFC fiber-connections**

There was a large correspondence of the fiber-connections between subject 1–11 and the respective point in time 1–7. There were inter-individual differences in particular with regard to the representation of the contralateral fiber-pathway via the AC (compare Figure 11 subject 5 TP 5 with subject 3 TP 3) or the visually-quantitatively recorded total fiber quantity within an ROI (compare Figure 12 subject 10 TP 4 with subject 8 TP 4).

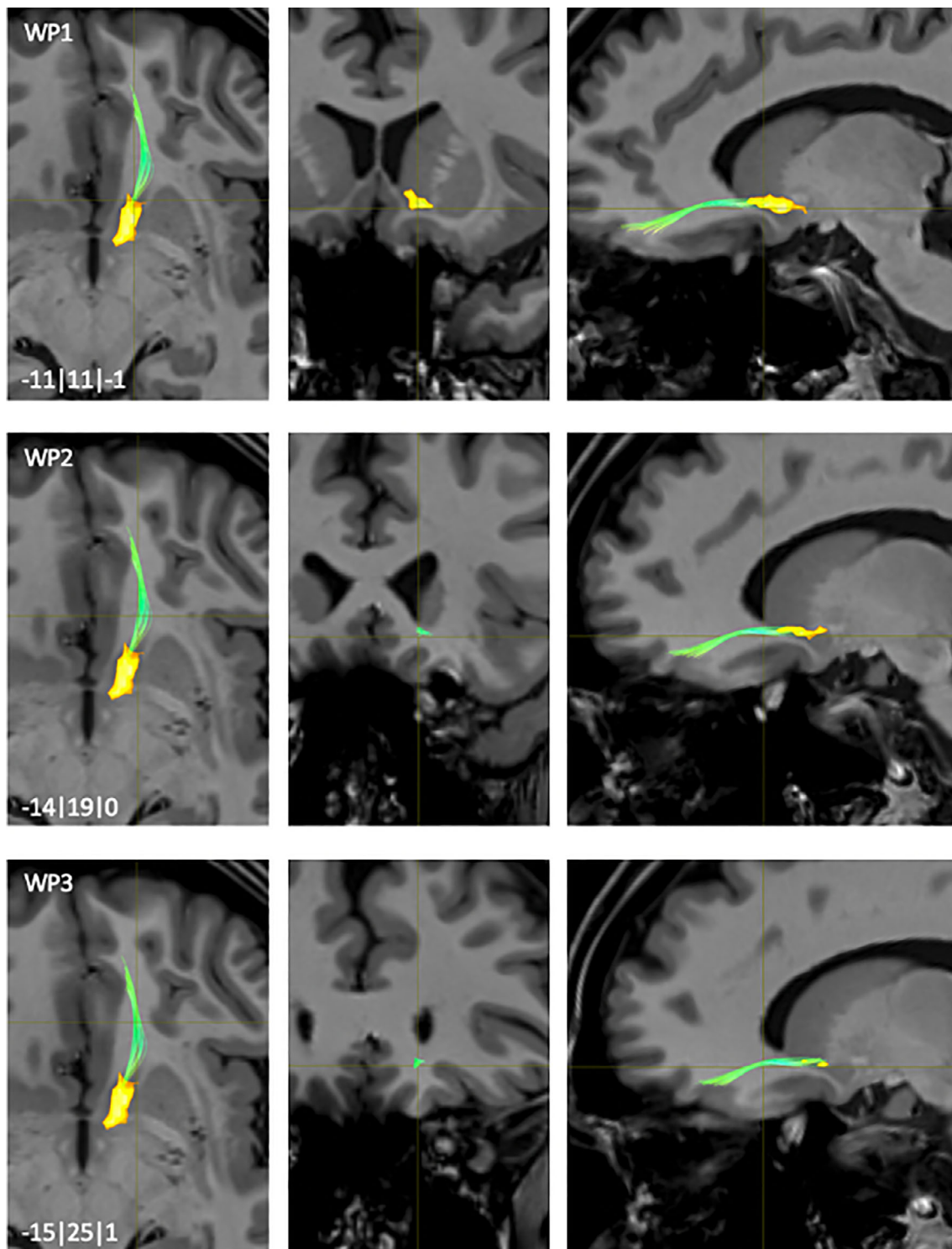


**FIGURE 8** NAc to mPFC fiber-tract for left hemisphere: Waypoint: 1–3 and distance to AC (0|0|0) in mm (x|y|z) = (left(-)/right|posterior (-)/anterior|inferior(-)/superior); yellow surface: NAc

## 4 | DISCUSSION

### 4.1 | Literature review

Tract-tracing and fiber-dissection studies are supposed to be the “gold-standards” for the visualization of neuronal fiber connections of the brain.

Naturally, these methods can only be applied in vivo. Fiber-tracking, the noninvasive alternative for clinical studies is error-prone for various reasons (Alhourani & Richardson, 2015). One systematic approach for a standardized segmentation and connectivity analysis, which can minimize the possible error sources is the determination of realistic functional and anatomical connections using the information from tract-tracing and fiber-

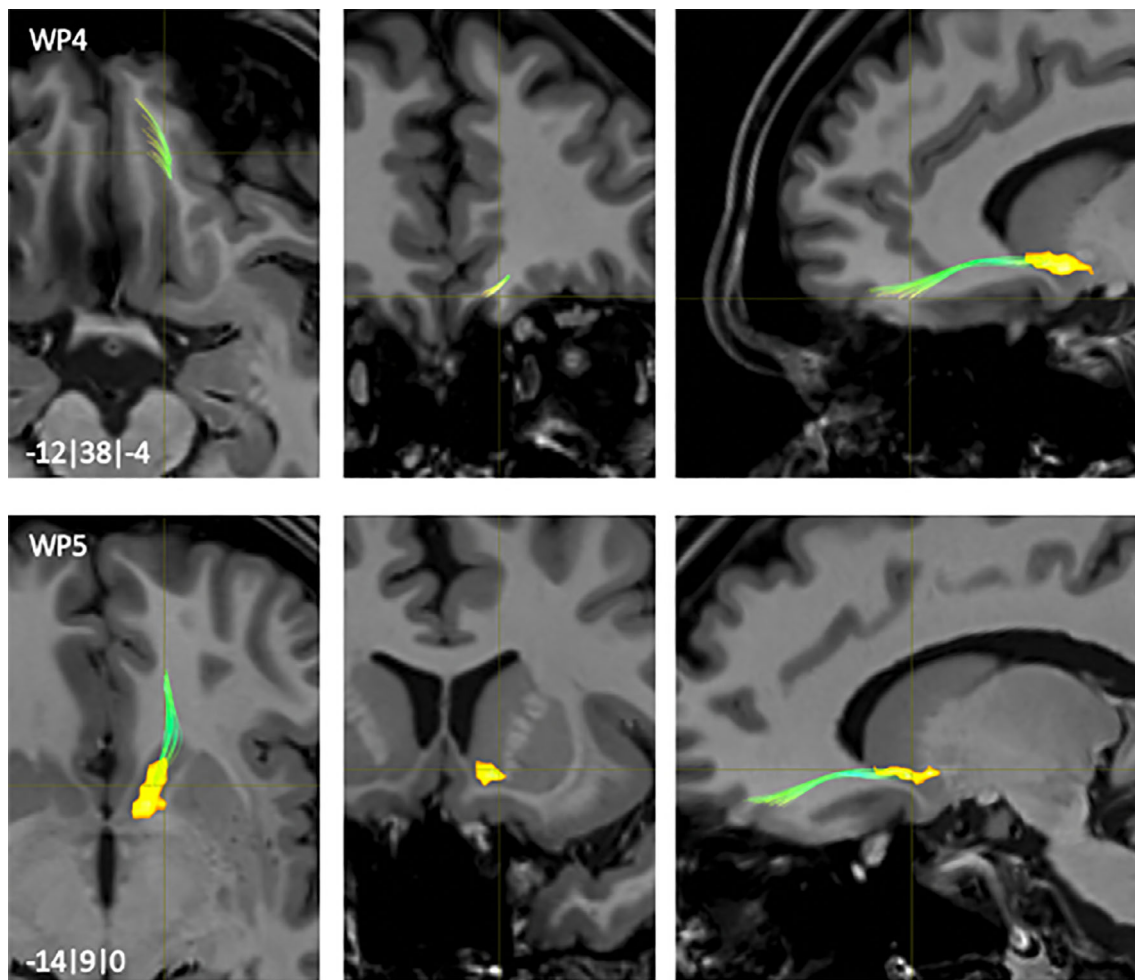


**FIGURE 9** NAc to mPFC fiber-tract for left hemisphere: Waypoint: 4–5 and distance to AC (0|0|0) in mm (x|y|z) = (left(-)/right|posterior (-)/anterior|inferior(-)/superior); yellow surface: NAc

dissection studies (Lambert et al., 2012). In preparation of the present analysis we extracted from a database containing to our knowledge the relevant literature all in vivo studies, which had reliably verified anatomical fiber connections, for example by tract-tracing. Afferences and efferences of the NAc determined in this way were concordant with results of published reviews addressing this topic (Neto, Oliveira, Correia, & Ferreira, 2008; Park et al., 2019; Salgado & Kaplitt, 2015; Sesack & Grace, 2010; Swanson & Cwan, 1975). The majority of the studies, which we had finally selected based on brain preparations of macaques and rodents. Even though the information obtained from these publications cannot be transferred to the human brain on a one-to-one basis, the start and end points of the defined fiber-connections correlated very well with the results of human-based studies (Saleem, Price, & Hashikawa, 2007; Salgado & Kaplitt, 2015; Tsao, Moeller, & Freiwald, 2008).

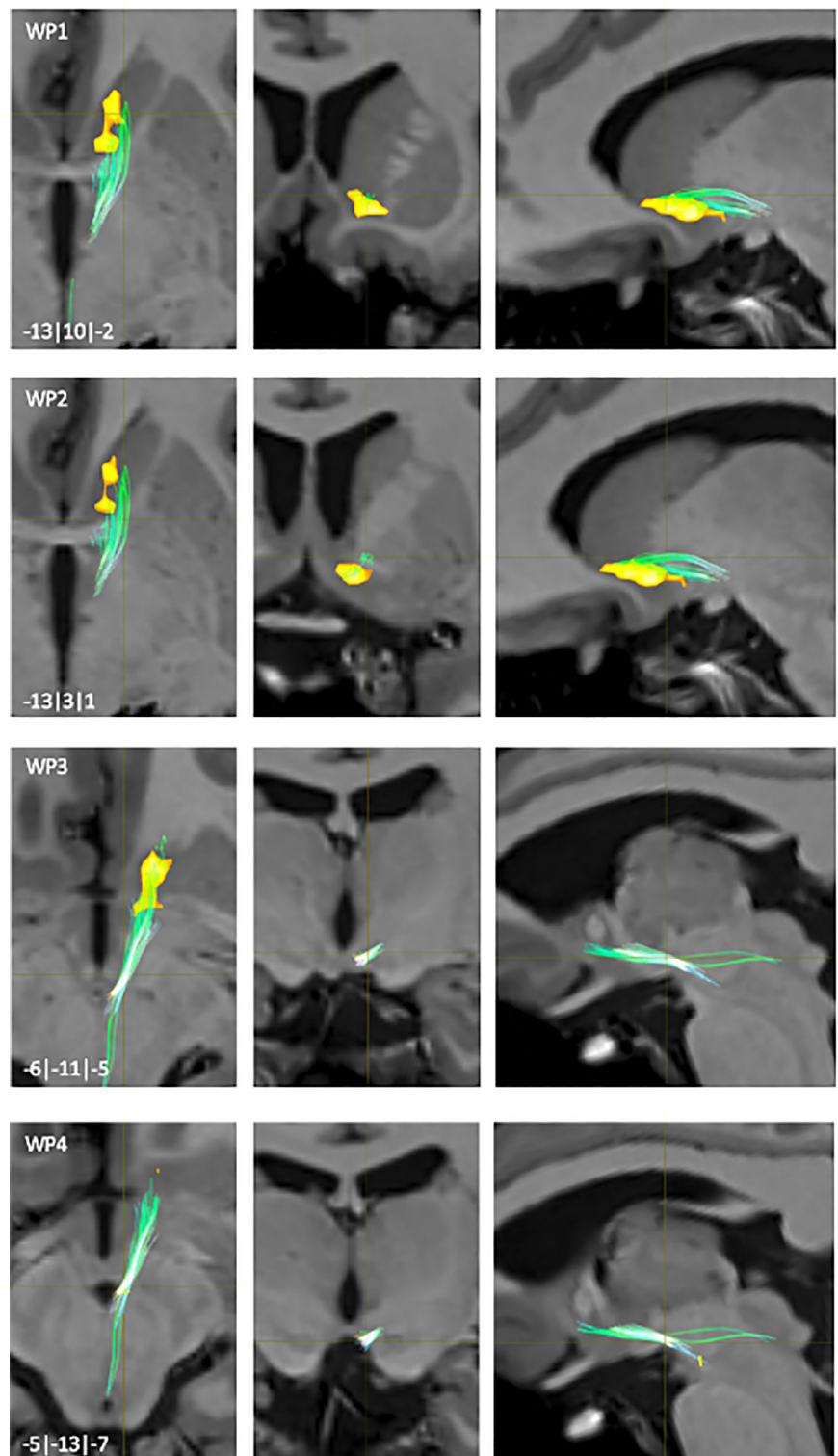
#### 4.2 | MRI-datasets, segmentation and fiber-tracking

The healthy subjects included in the present study had an average age of 29 years. Because of the low mean age combined with

unremarkable MRI-images at the time of study examination, structural changes of myelinated axons were almost excluded. This ensured reliable MRI-based imaging of NAc-connections of the healthy brain. In patients presenting with neuro-psychiatric or neurodegenerative diseases, however, the conditions could be different compared to the brains of healthy study participants. Structural changes associated, for instance, with brain atrophy can lead to focal changes in the fractional anisotropy and subsequent misinterpretation of diffusion-weighted MRI-based fiber-connections (Lacalle-Auriales et al., 2016). This problem will be addressed by our group in subsequent clinical studies.

The manual segmentation of the seed- and target-regions (VOIs) was carried out in the T1-single-subject-template (AMY, HPC, NAc) and FLAIR-single-subject-template (VTA) for each subject. The segmentation in the single-subject-templates instead of the T1- and FLAIR-single-subject-datasets had several advantages: The significantly higher signal-to-noise-ratio on the single-subject-templates compared to the single-subject measurements improved the recognition and delineation of anatomical structures. Since the segmentation was based on landmarks, we were able to define the boundaries of the VOIs more exactly, which reduced segmentation errors. As a consequence, the seed- and target-region had to be determined only

**FIGURE 10** NAc to VTA fiber-tract for left hemisphere: Waypoint: 1-3 and distance to AC (0|0|0) in mm (x|y|z) = (left(-)/right | posterior (-)/anterior | inferior(-)/superior); yellow surfaces: NAc, VTA



once per subject and could then automatically be transferred to the other measurement-timepoints using various calculation algorithms. In addition, the segmentation was not falsified by a potential intra-observer variability. Potential pitfalls of manual segmentation of anatomical VOIs causing inaccuracies to a certain degree are: The total number of segmented slices, the slice-level at the beginning or end of the segmentation, and/or the distinctness and visibility of the

boundaries of a particular VOI. Instructions for MRI-based manual segmentation were published for NAc (Lucas-Neto et al., 2015; Neto et al., 2008), AMY (Entis, Doerga, Barrett, & Dickerson, 2012) and HPC and were widely considered for the actual analysis. To our knowledge, MRI-based segmentation of the dmT or the VTA has not been published yet. Due to the lack of characteristic anatomical landmarks or boundaries, manual segmentation of cortex areas is

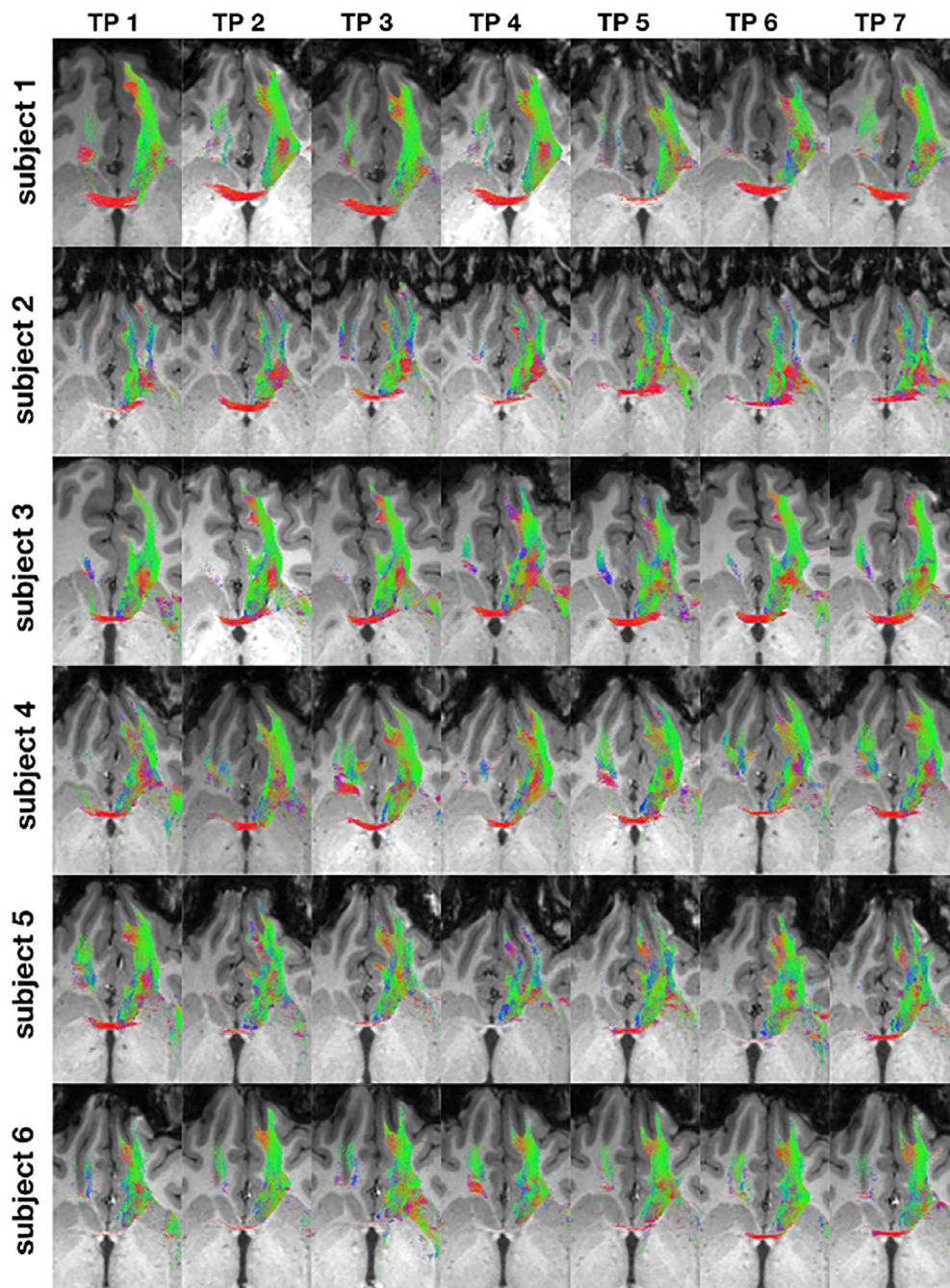


**FIGURE 11** NAc to VTA fiber-tract for left hemisphere: Waypoint: 4 and distance to AC (0|0|0) in mm (x|y|z) = (left (-)/right | posterior(-)/anterior | inferior(-)/superior); yellow surfaces: NAc, VTA

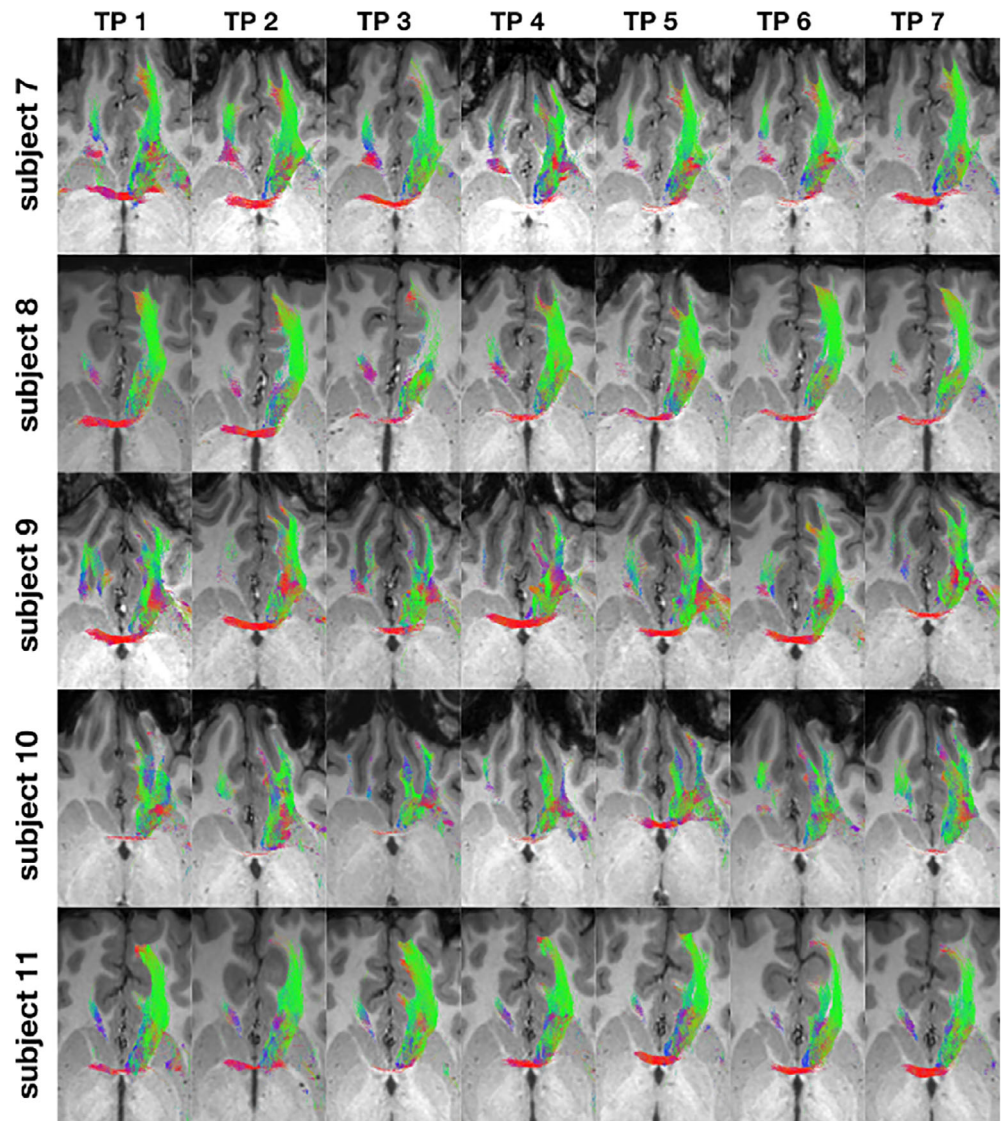
comparably difficult. Thus, we opted in the case of mPFC and ACC for automatic segmentation. The utilized software, however, permitted only segmentation based on previously defined sulci and gyri. Because published information on the overall extent of the mPFC is relatively inconsistent we used for the present analysis mPFC surface patterns and landmarks elaborated by Rodrigues et al. (Rodrigues et al., 2015).

The quality of diffusion-weighted MRI-based tractography is theoretically determined by various ex- and intrinsic errors. Major extrinsic errors are, for instance, various sources of interference, which naturally occur when MR-scans are taken from a living subject such as movement artifacts (e.g., heartbeat, breathing movements) and technical interference sources (eddy current distortions, susceptibility

artifacts). Appropriate computing algorithms such as the here used “FSL-Tool *eddy correct*” reduce these artifacts to a larger degree. Unfortunately, no data was acquired in reverse phase direction (P → A) during the initial subject measurements, so that processing steps such as FSL’s *topup/eddy* (Andersson, Skare, & Ashburner, 2003; Andersson & Sotiropoulos, 2016; Smith et al., 2004) could not be carried out. These are superior to the postprocessing method we used (application of field maps to reduce EPI- and susceptibility-induced distortions).

Another point is a method-related intrinsic blur caused by an unspecified diffusion profile of the corresponding water molecules in the area of the neuronal fibers, which cannot be modified by

**FIGURE 12** Fiber-connections NAc-mPFC for the left hemisphere of subject 7–11 for timepoint 1–7



postprocessing. Thomas et al. (2014) addressed this problem investigating the brain of macaques *ex-vivo* with extremely high-resolution diffusion-weighted MRI scans and various algorithms for tractography. Neuronal fiber-connections generated this way were finally compared with known axonal fiber-projections based on tract-tracing studies of the macaque's brain. Interestingly, independent from the applied tractography algorithm, the anatomical accuracy was insufficient. In particular, a high sensitivity of the generated fiber-connections (high rate correct-positive) corresponded to low specificity (high rate false-positive) and vice versa. Hence, the authors concluded, that an anatomically valid diffusion-weighted MRI-based fiber-pathway reconstruction was not sufficiently possible, especially if connections were not previously characterized. Consequently, they recommended verification and validation using corresponding postmortem tractography-data of either tract-tracing or fiber-dissection studies.

Further process-specific limitations of diffusion-weighted MRI-based tractography are:

1. No distinguishability between afferents and efferents of the reconstructed fiber-tracts.
2. Incorrect calculation of the main-diffusion vector at fiber crossing or branching points when using diffusion tensor imaging (DTI) based on a single tensor to describe multiple fibers within a single voxel (Auriat, Borich, Snow, Wadden, & Boyd, 2015; Basser, Pajevic, Pierpaoli, Duda, & Aldroubi, 2000).
3. Over-sprouting
 

The diffusion of water molecules parallel to neuronal pathways is higher than perpendicular to it. For this reason, detection of fiber-tracts by diffusion-weighted MRI is possible at all. A measurement of the exact direction of movement of the individual water molecules (forward or backward) is not possible, only that a change in location has occurred. Therefore, a distinction between afferents and efferents of diffusion-weighted MRI-based fiber-tracts is not possible, as mentioned under point 1. For a sufficient and detailed diffusion-weighted MRI based NAc fiber-tract reconstruction as the aim of this study, however, this is negligible. A labeling of the fiber-tract, whether it is an afference or efference, is ultimately carried out in correlation with the reviewed basic literature, for example tract-tracing studies.

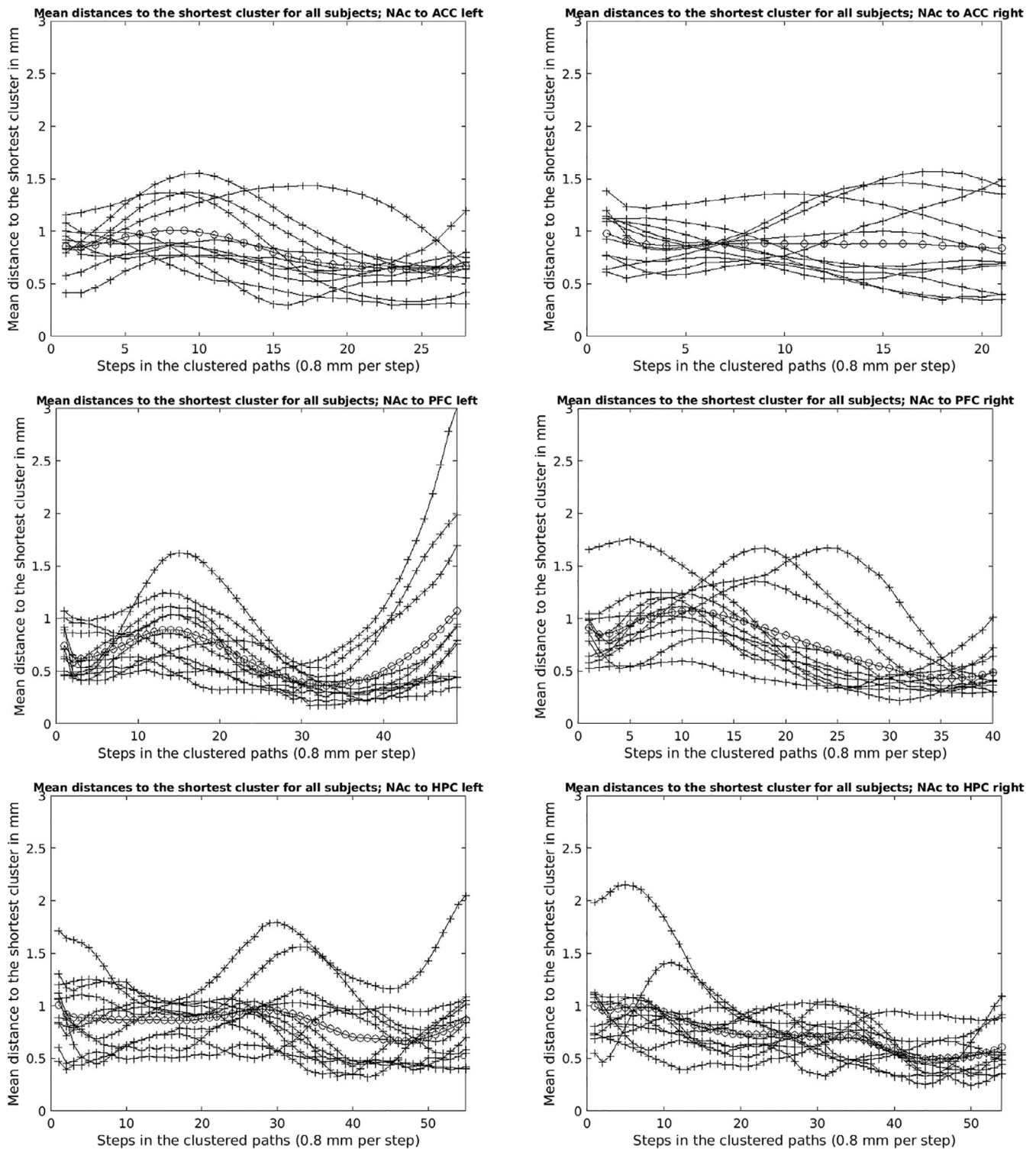


**FIGURE 13** Mean distances (lines with crosses) to the shortest cluster (TP 1–7) for all subjects 1–11 and overall average distance (line with circles) across all subjects (1–11) and TP 1–7 of the NAc to ACC, PFC and HPC fiber-connections for the left and right hemisphere in mm

To avoid an incorrect calculation of the main-diffusion vector at fiber-crossing or -branching points, as described in point 2, the outdated tensor model for modeling diffusion-weighted MRI based fiber-tracts is no longer used in the underlying study. Instead, a tensor-free orientation- and distribution-function is determined in each voxel

(constrained spherical deconvolution, CSD; see also 2.3.1. [Tournier, Calamante, & Connelly, 2007]) which is much more stable and sensitive to multiple intra-voxel fiber-pathway trajectories (Tournier, Mori, & Leemans, 2011). The more diffusion-directions are measured, which are distributed as evenly as possible on a spherical surface

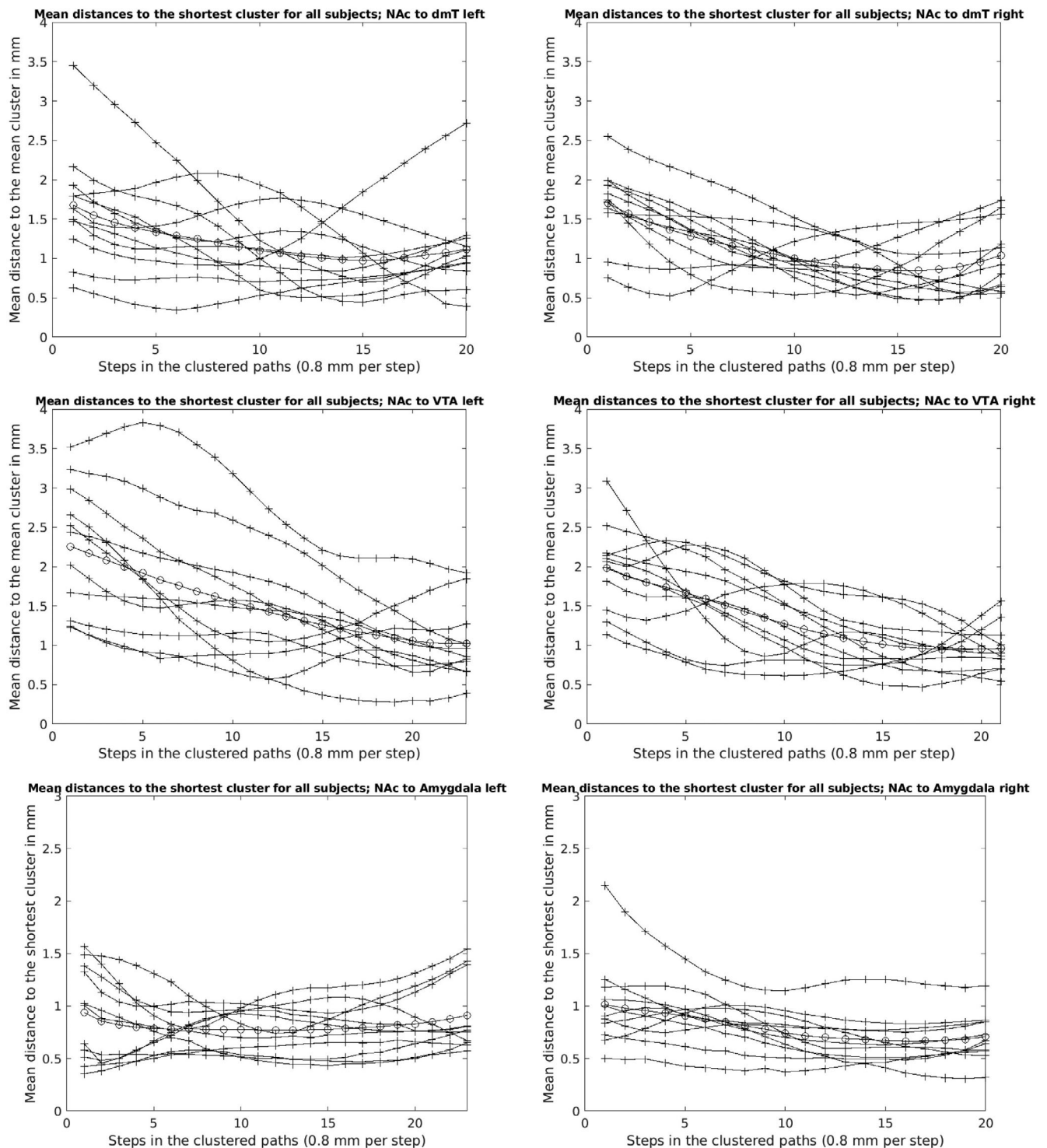


**FIGURE 14** Mean distances (lines with crosses) to the shortest cluster (TP 1–7) for all subjects 1–11 and overall average distance (line with circles) across all subjects (1–11) and TP 1–7 of the NAC to dmT, VTA and AMY fiber-connections for the left and right hemisphere in mm

(fiber orientation distribution, FOD [Tournier et al., 2007]), the more directions per voxel can be modeled. In addition, no information is lost, as is the case with the DTI-model, since here an average value of the individual single tensors is formed (Tournier et al., 2011). We measured 60 directions of diffusion.

Finally, if the maximum fiber-tract length in probabilistic fiber-tracking is chosen to high, this leads to incorrect fiber-tracts beyond the target structure (over-sprouting, point 3), fiber-loops or fiber-pathways via indirect relay-stations and thus incorrect diffusion-weighted MRI based fiber-reconstructions. To minimize this problem,

Subject	Hemisphere	Maximum Euclidian distances of single-clusters to the shortest single-cluster in mm						Average maximum Euclidian distances of single-clusters to the shortest single-cluster in mm					
		ACC	AMY	dmT	HPC	mPFC	VTA	ACC	AMY	dmT	HPC	mPFC	VTA
subject 1	left	2,70	1,58	5,45	2,40	1,32	6,30	1,19	0,77	3,45	0,97	0,52	2,44
subject 1	right	1,50	1,93	3,84	2,12	1,09	3,84	1,12	0,98	1,99	1,09	0,59	1,99
subject 2	left	2,12	2,08	3,42	2,08	3,40	5,68	1,00	1,39	2,08	1,12	1,69	2,99
subject 2	right	2,81	2,45	4,10	2,38	1,55	2,53	1,39	1,01	1,63	1,41	0,89	1,38
subject 3	left	2,28	1,87	4,08	3,26	1,52	2,62	0,91	0,93	2,72	1,15	0,79	1,31
subject 3	right	2,33	3,13	3,23	1,69	2,39	3,99	0,77	2,15	1,58	0,74	1,20	1,82
subject 4	left	3,34	1,92	2,42	4,52	1,60	4,64	1,37	0,68	0,94	2,05	0,79	2,66
subject 4	right	1,57	2,97	2,97	2,63	1,80	2,26	1,14	0,98	1,82	1,13	1,12	1,20
subject 5	left	2,57	2,14	3,11	1,75	3,91	4,23	1,08	1,02	1,49	1,01	3,02	1,67
subject 5	right	3,87	1,86	5,09	2,96	1,99	3,60	1,57	1,00	1,74	1,04	1,03	1,79
subject 6	left	2,27	2,86	4,18	2,40	1,39	4,67	1,55	1,49	1,93	0,94	0,94	2,52
subject 6	right	1,16	2,31	3,35	1,90	1,79	3,48	0,77	0,88	1,99	1,10	1,25	2,17
subject 7	left	2,24	2,71	5,71	3,49	2,80	6,35	0,92	1,57	1,79	1,30	1,99	3,83
subject 7	right	1,63	2,85	1,78	2,18	2,39	4,86	1,09	1,19	0,95	1,08	1,35	2,52
subject 8	left	1,95	2,54	3,08	5,50	1,84	2,38	0,95	1,38	1,77	1,72	0,92	1,23
subject 8	right	3,17	1,61	3,33	3,95	2,97	4,97	1,46	1,06	1,93	2,15	1,76	3,09
subject 9	left	2,97	1,31	2,03	1,96	4,31	3,88	1,37	0,65	0,95	1,08	1,04	1,24
subject 9	right	2,44	1,20	2,59	1,63	2,68	3,73	1,12	0,64	1,57	0,91	1,67	2,10
subject 10	left	1,53	1,50	4,42	2,98	2,07	4,57	0,77	1,09	2,17	1,56	1,11	2,02
subject 10	right	3,97	2,04	4,90	2,73	3,21	4,61	1,49	0,72	1,72	1,12	1,67	2,27
subject 11	left	2,27	1,82	2,64	1,91	2,01	4,75	1,43	1,00	1,47	1,25	1,04	3,23
subject 11	right	2,65	1,72	3,71	2,11	2,44	4,73	1,00	1,25	2,55	0,99	0,87	2,33
Maximum mean distances in mm	left							1,00	0,94	1,67	1,01	1,07	2,26
Maximum mean distances in mm	right							0,98	1,01	1,70	0,99	1,07	1,98

**FIGURE 15** Maximum Euclidian distances of single-clusters to the shortest single-cluster, average maximum Euclidian distances of single-clusters to the shortest single-cluster and maximum mean distances in mm for all NAc to target connections of each subject 1–11 (TP 1–7) for the right and left hemisphere

we tested different maximum fiber-lengths for each of the six seed-target-pairs, evaluated them optically and ultimately defined the optimal fiber-lengths for each specific fiber-connection.

### 4.3 | Anatomical validation of fiber-connections

In general, fiber-connections elaborated in the actual study matched closely relevant data on the course of fiber-pathways from in-vivo studies and from MRI-examinations of the human brain (Mori, 2005). More in detail, the course of a significant proportion of fibers from the NAc to the dmT running together with fibers of the stria medullaris thalami (sm) or of fiber-connections between NAc and ACC parallel to the ventral portion of the diagonal branch of Broca (VDB) has been described by Baydin et al. using fiber-dissection technique (Baydin, Yagmurlu, Tanriover, Gungor, & Rhoton Jr., 2016). Fiber-connection studies had also confirmed projections from the NAc to the mPFC. A more *medial* fiber bundle as identified in the present analysis, for instance, followed in rostral direction exactly the course of the fasciculus accumbens as described by Rigoard et al. (2011). Other fibers originating in the *medial* NAc with a dorso-lateral course and destination in the lateral AMY projected onto a connection, which was described by Baydin et al. and was according to Rigoard et al. synonym to the Fasciculus amygdaloaccumbens (Baydin et al., 2016; Rigoard et al., 2011). Also, the course of fibers with origin in *dorsal* parts of the NAc beside the septal area projecting onto the precommissural fornix and terminating in the HPC was confirmed by dissection studies (Baydin et al., 2016). Functionally, this pathway belongs to a hippocampo-prefrontal network, in which the NAc acts as a relay-station between the hippocampus and the PFC. For fiber-tracts connecting the NAc to the VTA in the present study we could not identify a morphological correlate in the current fiber-dissection-studies. However, MacNiven, Leong, and Knutson (2020) described two similar main fiber connections, which they refer to as inferior and

superior NAc-VTA tract in their DWI- and tractography-based structural analysis of the medial forebrain bundle and results from numerous tract-tracing-studies also confirmed this particular pathway (Beckstead, Domesick, & Nauta, 1979; Gorbachevskaya, 1991; Herkenham, Edley, & Stuart, 1984; Zahm & Heimer, 1993). Moreover, Coenen et al. had entirely characterized the medial forebrain bundle (MFB) for the human brain using MRI and global fiber-tracking (Coenen et al., 2018).

### 4.4 | Reliability and stability of fiber-connections

The data from the qualitative-visual intra-subject-comparison of the present study revealed an overall broad concordance with the fiber-pathway-anatomy reported in the literature. Intra-individual differences identified in the comparison analysis referred mainly to the total amount of fibers within specific fiber-tract sections. Three points could be responsible for this discrepancy: (i) With measurements at different timepoints it is impossible to keep exactly constant measurement conditions referred to position-differences, movement- and/or susceptibility artifacts. (ii) The calculation algorithms used for fiber-tracking are a probabilistic method, which can cause discrete differences. (iii) The number of calculated fibers might not necessarily correlate with the actual physical characteristics of the addressed fiber-pathway, an argument, which was raised by Nucifora, Verma, Melhem, Gur, and Gur (2005) and Vernooij et al. (2007) in context with the analysis of fiber-pathway-asymmetries of the Fasciculus arcuatus.

The methodology used for quantitative intra-subject-comparison in the present study was basically selected with respect to demonstrate stable reproducibility of the NAc fiber-tract-reconstructions and a prospective clinical application of the here elaborated workflow. For this purpose, the fiber-tracts of the individual NAc-to-target connections were clustered for each session 1–7 of subject 1–11 and finally the Euclidian distances of the single-clusters to the shortest

single-cluster were determined point by point. This made it possible to quantify the spatial deviations of the individual NAc-to-target connections between the individual sessions. The lower the distances, the better the spatial fiber-tract match and the higher the stability of the fiber-tracts under measurement repetition. As described in Section 2.3.2, for the sufficient clustering of some NAc-to-target connections (mPFC, ACC and HPC) an additional bundling/filtering of the fiber-tracts by defining specific ROIs was necessary. Because the ROIs were placed exclusively in the course of real fiber-tract points verified by our literature research of the basic anatomical literature and the MRI Atlas of Human White Matter (Mori, 2005), we do not consider this to represent arbitrary interference with the anatomy of the reconstructed fiber-tracts.

The largest maximum Euclidian distance of a single-cluster overall was 6.35 mm (see Figure 15) for the NAc-VTA-connection of subject 7 for the left hemisphere. A spatial fiber-trajectory deviation in measurement repetition in this size range would be critical for sufficient and accurate fiber-tracking based electrode positioning in DBS. However, it must be noted that the largest Euclidian distance of a single-cluster mentioned above is a point maximum value. This means that this value reflects the maximum fiber-pathway deviation of a single fiber-path section of all examined NAc-to-target-connections. Moreover, the Euclidian distances of the single-clusters were relatively high especially near the seed- (proximal fiber-pathway section) or target-regions (distal fiber-pathway section). This can be explained by the punctually different fiber trajectories exits (seed-region) or fiber trajectories entrances (target-region) and the resulting inhomogeneous clustering of the fibers at this location. However, since electrode placement immediately in the seed- or target-region is not favored (see current study situation in the text sections below), the larger Euclidian distances here are practically less problematic for diffusion-weighted based electrode positioning. Compared to the Euclidian distances of the single-clusters, the average Euclidian distances averaged over all sessions 1–7 of all subjects 1–11 (maximum mean distances) for the different NAc-to-target-connections were, however, distinctly lower. The maximum value corresponded to 2.26 mm for the NAc-VTA-connections of the left hemisphere. For some NAc-to-target-connections even <1 mm (NAc-ACC right hemisphere, NAc-AMY left hemisphere, NAc-HPC right hemisphere; see Figures 13–15). Overall, the individual NAc-fiber-tract-connections showed high stability and reproducibility. If a maximum deviation between intended (calculated) and final target of  $\leq 2$  mm is defined as precise for frame-based electrode positioning (Li, Zhang, Ye, & Li, 2016), then in the context of our tractography-based workflow, the average maximum total deviation would be  $\leq 4.26$  mm (provided we define the maximum average Euclidian distance of the NAc-VTA-connection of the left hemisphere (see above) as the maximum deviation to be assumed) and thus similarly feasible and safe compared with other studies investigating the accuracy of electrode placement in DBS (Burchiel, McCartney, Lee, & Raslan, 2013; Ferroli et al., 2004; Fiegele et al., 2008; Lumsden et al., 2013). Moreover, the white matter tract or fiber-tract identified as the target structure itself has a certain overall extent and therefore a volume. The fiber-tract reconstructed via diffusion-weighted-MRI

and subsequently clustered is line-shaped and does not represent a volume in this sense. Even in the case of spatial deviations of the single-clusters it can be assumed that they actually lie in the volume of the target structure. Independently, one would still perform a complementary visual inspection of the reconstructed fiber-tracts as part of surgical planning and identify major anatomic abnormalities, if any. In addition, the diffusion-weighted MRI-based electrode placement approach also highlights recent research findings that clinical outcome after DBS is better when directly stimulating the functional fiber-pathway rather than the target structure. For example, Fenoy and Schiess (2017) described better clinical results for reducing arm tremor when directly stimulating the dentato-rubro-thalamic tract instead stimulating the ventrolateral thalamus itself. Moreover, Leoutsakos et al. (2018) reported a possible positive clinical effect of direct bilateral stimulation of the fornix in mild Alzheimer-type dementia. Finally, in a noncontrolled study, Bewernick et al. (2012) showed that patients with severe refractory depression (major depressive disorder, MDD) improved significantly faster with direct electrical stimulation of the medial forebrain bundle (MFB) than with stimulation of the NAc, ventral striatum (VS)/ventral capsule (VC), or anterior limb of the internal capsule (aic). Once achieved, the positive effect on depression was stable over the long-term. The same working group already pointed out in 2017 that possibly also in OCD-patients (OCD = obsessive-compulsive disorder) direct MFB-DBS could be more effective than electrical stimulation of the brain areas (NAc, VS/VC, aic) previously approved for treatment. This observation is supported by data recently published by Liebrand et al. (2019). These authors reported a correlation between the response of OCD-symptoms and the distance of the active electrode contacts to fibers of the MFB (shorter distance = better outcome) in DBS of the ventral portion of the aic for the treatment of OCD.

In addition, as part of the quantitative intra-subject-comparison, we evaluated additional parameters aiming at the statistical comparability of diffusion-weighted based fiber-reconstructions (fractional anisotropy [FA-maps] and density-maps). Since the number of fibers and the fiber-pathway within a defined VOI depend on many different framework conditions (e.g., movement and susceptibility artifacts), these parameters were not robust enough from this point of view to provide conclusive results. This experience was in line with statements formulated by Bartlett and Frost (2008), who addressed in their work the analysis of measurement errors in the context of reliability.

## 5 | CONCLUSIONS

In the present study, we were able to visualize reproducible, precise and very specific projections from and to the NAc using DWI-MRI and fiber-tracking. A limitation of this work is the fact that the fiber reconstructions based on young and healthy subjects. Further investigations on patients will clarify if older age and associated brain atrophy or neuropsychiatric diseases reducing the volume of the NAc such in heroin addicts may influence the stability and validity of fiber reconstructions (Muller et al., 2015). The methodological workflow

developed for the present study could be prospectively implemented in the clinical routine for stereotactic treatment planning and could selectively guide the implantation of DBS-brain electrodes into the NAc. Besides local effects in the immediate vicinity to the stimulation site DBS is supposed to have preferentially a modulatory impact on diseased neuronal networks favoring myelinated axons and hence white matter as target structures (Ashkan, Rogers, Bergman, & Ughratdar, 2017; Ranck Jr., 1975).

Functional neuroimaging and connectivity analyses gave some hints that the clinical heterogeneity of OCD, for instance, is linked to distinct neural correlates (Senova et al., 2019) implying selective electrical stimulation of fiber connections depending on the individual symptom or neurocognitive pattern. Hence, diffusion-weighted MRI-based visualization of distinct fiber-connections for a more personalized placement of DBS brain electrodes seems logical.

#### DATA AVAILABILITY STATEMENT

Data available on request from the authors.

#### ORCID

Thilo Rusche  <https://orcid.org/0000-0002-8712-5759>

#### REFERENCES

- Alhourani, A., & Richardson, R. M. (2015). Inherent limitations of tractography for accurate connectivity maps. *Neurosurgery*, *76*, N11–N12.
- Andersson, J. L., Skare, S., & Ashburner, J. (2003). How to correct susceptibility distortions in spin-echo echo-planar images: Application to diffusion tensor imaging. *NeuroImage*, *20*, 870–888.
- Andersson, J. L. R., & Sotiropoulos, S. N. (2016). An integrated approach to correction for off-resonance effects and subject movement in diffusion MR imaging. *NeuroImage*, *125*, 1063–1078.
- Ashkan, K., Rogers, P., Bergman, H., & Ughratdar, I. (2017). Insights into the mechanisms of deep brain stimulation. *Nature Reviews. Neurology*, *13*, 548–554.
- Auriat, A. M., Borich, M. R., Snow, N. J., Wadden, K. P., & Boyd, L. A. (2015). Comparing a diffusion tensor and non-tensor approach to white matter fiber tractography in chronic stroke. *NeuroImage: Clinical*, *7*, 771–781.
- Avants, B. B., Yushkevich, P., Pluta, J., Minkoff, D., Korczykowski, M., Detre, J., & Gee, J. C. (2010). The optimal template effect in hippocampus studies of diseased populations. *NeuroImage*, *49*, 2457–2466.
- Bartlett, J. W., & Frost, C. (2008). Reliability, repeatability and reproducibility: Analysis of measurement errors in continuous variables. *Ultrasound in Obstetrics & Gynecology*, *31*, 466–475.
- Basser, P. J., Pajevic, S., Pierpaoli, C., Duda, J., & Aldroubi, A. (2000). In vivo fiber tractography using DT-MRI data. *Magnetic Resonance in Medicine*, *44*, 625–632.
- Baydin, S., Yagmurlu, K., Tanriover, N., Gungor, A., & Rhoton, A. L., Jr. (2016). Microsurgical and fiber tract anatomy of the nucleus accumbens. *Operative Neurosurgery (Hagerstown)*, *12*, 269–288.
- Beckstead, R. M., Domesick, V. B., & Nauta, W. J. (1979). Efferent connections of the substantia nigra and ventral tegmental area in the rat. *Brain Research*, *175*, 191–217.
- Bewernick, B. H., Kayser, S., Sturm, V., & Schlaepfer, T. E. (2012). Long-term effects of nucleus accumbens deep brain stimulation in treatment-resistant depression: Evidence for sustained efficacy. *Neuropsychopharmacology*, *37*, 1975–1985.
- Burchiel, K. J., McCartney, S., Lee, A., & Raslan, A. M. (2013). Accuracy of deep brain stimulation electrode placement using intraoperative computed tomography without microelectrode recording. *Journal of Neurosurgery*, *119*, 301–306.
- Coenen, V. A., Schumacher, L. V., Kaller, C., Schlaepfer, T. E., Reinacher, P. C., Egger, K., ... Reiser, M. (2018). The anatomy of the human medial forebrain bundle: Ventral tegmental area connections to reward-associated subcortical and frontal lobe regions. *NeuroImage: Clinical*, *18*, 770–783.
- Dale, A. M., Fischl, B., & Sereno, M. I. (1999). Cortical surface-based analysis. I. Segmentation and surface reconstruction. *NeuroImage*, *9*, 179–194.
- Denys, D., Mantione, M., Figeo, M., van den Munckhof, P., Koerselman, F., Westenberg, H., ... Schuurman, R. (2010). Deep brain stimulation of the nucleus accumbens for treatment-refractory obsessive-compulsive disorder. *Archives of General Psychiatry*, *67*, 1061–1068.
- Entis, J. J., Doerga, P., Barrett, L. F., & Dickerson, B. C. (2012). A reliable protocol for the manual segmentation of the human amygdala and its subregions using ultra-high resolution MRI. *NeuroImage*, *60*, 1226–1235.
- Fenoy, A. J., & Schiess, M. C. (2017). Deep brain stimulation of the dentato-rubro-thalamic tract: Outcomes of direct targeting for tremor. *Neuromodulation*, *20*, 429–436.
- Ferrolì, P., Franzini, A., Marras, C., Maccagnano, E., D'Incerti, L., & Broggi, G. (2004). A simple method to assess accuracy of deep brain stimulation electrode placement: Pre-operative stereotactic CT + postoperative MR image fusion. *Stereotactic and Functional Neurosurgery*, *82*, 14–19.
- Fiegele, T., Feuchtner, G., Sohm, F., Bauer, R., Anton, J. V., Gotwald, T., ... Eisner, W. (2008). Accuracy of stereotactic electrode placement in deep brain stimulation by intraoperative computed tomography. *Parkinsonism & Related Disorders*, *14*, 595–599.
- Forel, A. (1875). Untersuchungen über die Haubenregion und ihre obere Verknüpfung im Gehirne des Menschen und einiger Säugetiere, mit Beiträgen zu den Methoden der Gehirnuntersuchung. *Archives of General Psychiatry*, *7*(3), 26–495.
- Giacobbe, P., Mayberg, H. S., & Lozano, A. M. (2009). Treatment resistant depression as a failure of brain homeostatic mechanisms: Implications for deep brain stimulation. *Experimental Neurology*, *219*, 44–52.
- Gorbachevskaya, A. I. (1991). Afferent connections of the nucleus accumbens with the amygdaloid body and the dopaminergic mesencephalic formations of the cat brain. *Neuroscience and Behavioral Physiology*, *21*, 540–546.
- Graham, M. S., Drobnyak, I., & Zhang, H. (2016). Realistic simulation of artefacts in diffusion MRI for validating post-processing correction techniques. *NeuroImage*, *125*, 1079–1094.
- Griswold, M. A., Jakob, P. M., Heidemann, R. M., Nittka, M., Jellus, V., Wang, J., ... Haase, A. (2002). Generalized autocalibrating partially parallel acquisitions (GRAPPA). *Magnetic Resonance in Medicine*, *47*, 1202–1210.
- Haber, S. N., & Behrens, T. E. (2014). The neural network underlying incentive-based learning: Implications for interpreting circuit disruptions in psychiatric disorders. *Neuron*, *83*, 1019–1039.
- Haber, S. N., & McFarland, N. R. (1999). The concept of the ventral striatum in nonhuman primates. *Annals of the New York Academy of Sciences*, *877*, 33–48.
- Heimer, L. (2003). A new anatomical framework for neuropsychiatric disorders and drug abuse. *The American Journal of Psychiatry*, *160*, 1726–1739.
- Herkenham, M., Edley, S. M., & Stuart, J. (1984). Cell clusters in the nucleus accumbens of the rat, and the mosaic relationship of opiate receptors, acetylcholinesterase and subcortical afferent terminations. *Neuroscience*, *11*, 561–593.
- Herrington, T. M., Cheng, J. J., & Eskandar, E. N. (2016). Mechanisms of deep brain stimulation. *Journal of Neurophysiology*, *115*, 19–38.

- Jenkinson, M., Beckmann, C. F., Behrens, T. E., Woolrich, M. W., & Smith, S. M. (2012). Fsl. *NeuroImage*, 62, 782–790.
- Jones, D. K., & Cercignani, M. (2010). Twenty-five pitfalls in the analysis of diffusion MRI data. *NMR in Biomedicine*, 23, 803–820.
- Kellner, E., Dhital, B., Kiselev, V. G., & Reiser, M. (2016). Gibbs-ringing artifact removal based on local subvoxel-shifts. *Magnetic Resonance in Medicine*, 76, 1574–1581.
- Kowski, A. B., Voges, J., Heinze, H. J., Oltmanns, F., Holtkamp, M., & Schmitt, F. C. (2015). Nucleus accumbens stimulation in partial epilepsy—A randomized controlled case series. *Epilepsia*, 56, e78–e82.
- Lacalle-Auriales, M., Navas-Sanchez, F. J., Aleman-Gomez, Y., Olazaran, J., Guzman-De-Villoria, J. A., Cruz-Orduna, I., ... Desco, M. (2016). The disconnection hypothesis in Alzheimer's disease studied through multimodal magnetic resonance imaging: Structural, perfusion, and diffusion tensor imaging. *Journal of Alzheimer's Disease*, 50, 1051–1064.
- Lambert, C., Zrinzo, L., Nagy, Z., Lutti, A., Hariz, M., Foltynie, T., ... Frackowiak, R. (2012). Confirmation of functional zones within the human subthalamic nucleus: Patterns of connectivity and sub-parcellation using diffusion weighted imaging. *NeuroImage*, 60, 83–94.
- Leoutsakos, J. S., Yan, H., Anderson, W. S., Asaad, W. F., Baltuch, G., Burke, A., ... Lyketsos, C. G. (2018). Deep brain stimulation targeting the fornix for mild Alzheimer dementia (the ADVance trial): A two year follow-up including results of delayed activation. *Journal of Alzheimer's Disease*, 64, 597–606.
- Li, Z., Zhang, J. G., Ye, Y., & Li, X. (2016). Review on factors affecting targeting accuracy of deep brain stimulation electrode implantation between 2001 and 2015. *Stereotactic and Functional Neurosurgery*, 94, 351–362.
- Liebrand, L. C., Caan, M. W. A., Schuurman, P. R., van den Munckhof, P., Fiege, M., Denys, D., & van Wingen, G. A. (2019). Individual white matter bundle trajectories are associated with deep brain stimulation response in obsessive-compulsive disorder. *Brain Stimulation*, 12, 353–360.
- Lucas-Neto, L., Reimao, S., Oliveira, E., Rainha-Campos, A., Sousa, J., Nunes, R. G., ... Campos, J. G. (2015). Advanced MR imaging of the human nucleus accumbens—Additional guiding tool for deep brain stimulation. *Neuromodulation*, 18, 341–348.
- Lumsden, D. E., Ashmore, J., Charles-Edwards, G., Lin, J. P., Ashkan, K., & Selway, R. (2013). Accuracy of stimulating electrode placement in paediatric pallidal deep brain stimulation for primary and secondary dystonia. *Acta Neurochirurgica*, 155, 823–836.
- MacNiven, K. H., Leong, J. K., & Knutson, B. (2020). Medial forebrain bundle structure is linked to human impulsivity. *Science Advances*, 6, eaba4788.
- Mai, J. K., Voss, T., & Paxinos, G. (2008). *Atlas of the human brain*. Amsterdam; Boston: Elsevier/Academic Press.
- Milad, M. R., & Rauch, S. L. (2012). Obsessive-compulsive disorder: Beyond segregated cortico-striatal pathways. *Trends in Cognitive Sciences*, 16, 43–51.
- Mori, S. (2005). *MRI atlas of human white matter*. Amsterdam, Oxford: Elsevier.
- Muller, U. J., Truebner, K., Schiltz, K., Kuhn, J., Mawrin, C., Dobrowolny, H., ... Steiner, J. (2015). Postmortem volumetric analysis of the nucleus accumbens in male heroin addicts: Implications for deep brain stimulation. *European Archives of Psychiatry and Clinical Neuroscience*, 265, 647–653.
- Neto, L. L., Oliveira, E., Correia, F., & Ferreira, A. G. (2008). The human nucleus accumbens: Where is it? A stereotactic, anatomical and magnetic resonance imaging study. *Neuromodulation*, 11, 13–22.
- Nucifora, P. G., Verma, R., Melhem, E. R., Gur, R. E., & Gur, R. C. (2005). Leftward asymmetry in relative fiber density of the arcuate fasciculus. *Neuroreport*, 16, 791–794.
- Park, Y. S., Sammartino, F., Young, N. A., Corrigan, J., Krishna, V., & Reza, A. R. (2019). Anatomic review of the ventral capsule/ventral striatum and the nucleus accumbens to guide target selection for deep brain stimulation for obsessive-compulsive disorder. *World Neurosurgery*, 126, 1–10.
- Ranck, J. B., Jr. (1975). Which elements are excited in electrical stimulation of mammalian central nervous system: A review. *Brain Research*, 98, 417–440.
- Ressler, K. J., & Mayberg, H. S. (2007). Targeting abnormal neural circuits in mood and anxiety disorders: From the laboratory to the clinic. *Nature Neuroscience*, 10, 1116–1124.
- Rigoard, P., Buffenoir, K., Jaafari, N., Giot, J. P., Houeto, J. L., Mertens, P., ... Bataille, B. (2011). The accumbens fasciculus in the human brain: A microsurgical anatomical study. *Neurosurgery*, 68, 1102–1111 discussion 11.
- Rodrigues, T. P., Rodrigues, M. A., Paz Dde, A., Costa, M. D., Centeno, R. S., Chaddad Neto, F. E., & Cavalheiro, S. (2015). Orbitofrontal sulcal and gyrus pattern in human: An anatomical study. *Arquivos de Neuro-Psiquiatria*, 73, 431–435.
- Saleem, K. S., Price, J. L., & Hashikawa, T. (2007). Cytoarchitectonic and chemoarchitectonic subdivisions of the perirhinal and parahippocampal cortices in macaque monkeys. *The Journal of Comparative Neurology*, 500, 973–1006.
- Salgado, S., & Kaplitt, M. G. (2015). The nucleus accumbens: A comprehensive review. *Stereotactic and Functional Neurosurgery*, 93, 75–93.
- Schmitt, F. C., Voges, J., Heinze, H. J., Zaehle, T., Holtkamp, M., & Kowski, A. B. (2014). Safety and feasibility of nucleus accumbens stimulation in five patients with epilepsy. *Journal of Neurology*, 261, 1477–1484.
- Senova, S., Clair, A. H., Palfi, S., Yelnik, J., Domenech, P., & Mallet, L. (2019). Deep brain stimulation for refractory obsessive-compulsive disorder: Towards an individualized approach. *Frontiers in Psychiatry*, 10, 905.
- Sesack, S. R., & Grace, A. A. (2010). Cortico-basal ganglia reward network: Microcircuitry. *Neuropsychopharmacology*, 35, 27–47.
- Smith, R. E., Tournier, J. D., Calamante, F., & Connelly, A. (2012). Anatomically-constrained tractography: Improved diffusion MRI streamlines tractography through effective use of anatomical information. *NeuroImage*, 62, 1924–1938.
- Smith, S. M., Jenkinson, M., Woolrich, M. W., Beckmann, C. F., Behrens, T. E., Johansen-Berg, H., ... Matthews, P. M. (2004). Advances in functional and structural MR image analysis and implementation as FSL. *NeuroImage*, 23(Suppl. 1), S208–S219.
- Sturm, V., Lenartz, D., Koulousakis, A., Treuer, H., Herholz, K., Klein, J. C., & Klosterkötter, J. (2003). The nucleus accumbens: A target for deep brain stimulation in obsessive-compulsive- and anxiety-disorders. *Journal of Chemical Neuroanatomy*, 26, 293–299.
- Swanson, L. W., & Cwan, W. M. (1975). A note on the connections and development of the nucleus accumbens. *Brain Research*, 92, 324–330.
- Thomas, C., Ye, F. Q., Irfanoglu, M. O., Modi, P., Saleem, K. S., Leopold, D. A., & Pierpaoli, C. (2014). Anatomical accuracy of brain connections derived from diffusion MRI tractography is inherently limited. *Proceedings of the National Academy of Sciences of the United States of America*, 111, 16574–16579.
- Tournier, J. D., Calamante, F., & Connelly, A. (2007). Robust determination of the fibre orientation distribution in diffusion MRI: Non-negativity constrained super-resolved spherical deconvolution. *NeuroImage*, 35, 1459–1472.
- Tournier, J. D., Mori, S., & Leemans, A. (2011). Diffusion tensor imaging and beyond. *Magnetic Resonance in Medicine*, 65, 1532–1556.
- Tournier, J. D., Smith, R., Raffelt, D., Tabbara, R., Dhollander, T., Pietsch, M., ... Connelly, A. (2019). MRtrix3: A fast, flexible and open software framework for medical image processing and visualisation. *NeuroImage*, 202, 116137.
- Tsao, D. Y., Moeller, S., & Freiwald, W. A. (2008). Comparing face patch systems in macaques and humans. *Proceedings of the National Academy of Sciences of the United States of America*, 105, 19514–19519.
- Udupa, K., & Chen, R. (2015). The mechanisms of action of deep brain stimulation and ideas for the future development. *Progress in Neurobiology*, 133, 27–49.
- Vernooij, M. W., Smits, M., Wielopolski, P. A., Houston, G. C., Krestin, G. P., & van der Lugt, A. (2007). Fiber density asymmetry of the arcuate fasciculus in relation to functional hemispheric language

- lateralization in both right- and left-handed healthy subjects: A combined fMRI and DTI study. *NeuroImage*, 35, 1064–1076.
- Voges, J., Muller, U., Bogerts, B., Munte, T., & Heinze, H. J. (2013). Deep brain stimulation surgery for alcohol addiction. *World Neurosurgery*, 80(S28), e21–e31.
- Zahm, D. S., & Heimer, L. (1993). Specificity in the efferent projections of the nucleus accumbens in the rat: Comparison of the rostral pole projection patterns with those of the core and shell. *The Journal of Comparative Neurology*, 327, 220–232.

**How to cite this article:** Rusche, T., Kaufmann, J., & Voges, J. (2021). Nucleus accumbens projections: Validity and reliability of fiber reconstructions based on high-resolution diffusion-weighted MRI. *Human Brain Mapping*, 42(18), 5888–5910. <https://doi.org/10.1002/hbm.25657>